# The observed spatiotemporal variability of Antarctic Winter Water

**T. Spira[1], S. Swart[1,2], I. Giddy[1], M. du Plessis[1]**

[1]Department of Marine Sciences, University of Gothenburg, Sweden
[2]Department of Oceanography, University of Cape Town, Rondebosch, South Africa

**Key Points:**

- Seasonal climatologies of Antarctic Winter Water (WW) and its properties are mapped using 18 years of in-situ observations.
- Observations reveal the distinct seasonal and regional characteristics of WW and their connections to processes such as sea-ice formation.
- Localized redistribution of WW properties equatorward is steered by large topographic features.

Corresponding author: Theo Spira, `theo.spira@gu.se`

## Abstract

The Southern Ocean is central to the global overturning circulation. South of the Antarctic Polar Front, Antarctic Winter Water (WW) forms in the wintertime mixed layer below sea ice and becomes a subsurface layer following summertime restratification of the mixed layer, overlaying upwelled deep waters. Model simulations show that WW acts as a conduit to seasonally transform upwelled deep waters into intermediate waters. Yet, there remains little observational evidence of the distribution and seasonal characteristics of WW. Using 18 years of in situ observations, we show seasonal climatologies of WW thickness, depth, core temperature and salinity. This study reveals, for the first time, the distinct regionality and seasonality of WW. The seasonal cycle of WW characteristics is tied to the annual sea ice evolution, whilst the spatial distribution is impacted by the main topographic features in the Southern Ocean driving an equatorward flux of WW. Through the identification of these localized northward export regions of WW, this study provides further evidence suggesting an alternative view from the conventional 'zonal mean' perspective of the overturning circulation. We show that specific overturning pathways connecting the subpolar ocean to the global ocean can be explained by ocean-topography interactions.


## Plain Language Summary

The Southern Ocean around Antarctica is central to the global ocean circulation system. The cold wintertime atmosphere drives ocean cooling and sea ice formation, which causes surface waters to become denser, mixing with deep waters that rise to the surface from the deep ocean. As the ocean surface layer warms in summer, there remains a cold layer below the surface known as Antarctic Winter Water (WW). This layer warms throughout the summer, thinning the WW layer. However, the properties of WW (temperature, salinity, thickness, depth) vary in space around the Southern Ocean and in erosion rate. By compiling 18 years of ocean observations, we investigate the physical dynamics that determine how WW changes in space and over the average annual cycle. We find that there are localized regions across the Southern Ocean where WW properties are transported northwards as part of the ocean circulation system, which typically align with large topographic features and act to connect Southern Ocean water masses to the global ocean.

## 1 Introduction

The Southern Ocean (SO) is characterized by the zonally unbounded energetic flow of the Antarctic Circumpolar Current (ACC), which consists of several baroclinic jets that delineate hydrographic properties (Orsi et al., 1995). South of the Antarctic Polar Front, salinity is the dominant property of density in the upper ocean due to a low thermal expansion coefficient (Stewart & Haine, 2016; Roquet et al., 2022). Consequently, this allows for the formation of a cold subsurface layer known as Antarctic Winter Water (AAWW; henceforth WW) that resides below the summertime mixed layer (Toole, 1981).

WW lies above the salty and relatively warm Circumpolar Deep Water (CDW), which has been upwelled along isopycnals from the deep ocean (Tamsitt et al., 2017). CDW gets transformed to become either dense bottom water in the southern upwelling limb, sinking back to the abyssal ocean (Ganachaud & Wunsch, 2000; Jacobs, 2004; van Sebille et al., 2013), or transformed to intermediate water north of the ACC (Munk, 1966; Whitworth et al., 1994). Evans et al. (2018) showed, using a general circulation model, that WW acts as a seasonal conduit to connect CDW to Antarctic Intermediate Water in summertime which, when subducted, forms the downwelling limb of the SO meridional overturning circulation (Speer et al., 2000; Marshall & Speer, 2012; Talley, 2013). Water mass transformation in the upper SO is associated with net freshening due to sea ice export and melt (Abernathey et al., 2016; Pellichero et al., 2018), and Tamsitt et al. (2018) showed that upwelled CDW becomes fresher and colder before transforming into intermediate waters, further implying the seasonal role of WW in the overturning circulation. Drake et al. (2018) show through investigation of Lagrangian pathways that CDW upwelling is not well represented via the time mean overturning framework, and thus, by implication, a similar argument likely applies to the representation of WW in the same zonally integrated overturning framework. Given these findings, the evolution and characteristics of WW are important to the overall SO's role in the global overturning circulation.

WW forms in the wintertime mixed layer (ML; Figure 1a), which deepens through buoyancy loss via cooling and sea ice formation. Brine rejection deepens the under-ice ML, driving entrainment of the warm subsurface CDW and thus increases ML heat and salinity (Gordon & Huber, 1984). In turn, this melts sea ice and freshens the ML to reduce its buoyancy; thus, through this feedback system, sea ice thickness is maintained as relatively thin ($\sim$0.5 m) (Shaw & Stanton, 2014) and the under-ice ML is generally confined to less than 200 m depth (Martinson, 1990; Biddle & Swart, 2020; Wilson et al., 2019). Following a change in sign of the atmospheric heat flux, the summertime ML shoals becoming warm and fresh with a depth of only tens of meters (Pellichero et al., 2017), leaving a residual subsurface cold wintertime ML below the summer-warmed surface layer (Figure 1b) and thus creating a warm-cold-warm layering of ML-WW-CDW (Park, Charriaud, & Fieux, 1998).

Eventually, WW erodes over the annual cycle or is re-entrained into the following winter ML. Giddy et al. (2023) found that WW erosion rates are primarily driven by entrainment of WW into the mixed layer through mechanical mixing, with further warming due to double diffusive convection from below. However, these findings are specific to the Weddell Sea where there is typically a sharp thermocline yet a weak pycnocline (Wilson et al., 2019), which impacts the temperature gradient as well as the rate of mixing that takes place. Further, variability of WW properties have been observed in regions up- and downstream of large topographic features that interact with the ACC, enhancing the downstream mesoscale field, such as that found by Sabu et al. (2020). Lund et al. (2021) show similar spatial variability across the circumpolar SO via climatological WW temperatures. Sabu et al. (2020) also observe the WW layer responding to large-scale atmospheric variability, finding enhanced warming in years of positive Southern Annular Mode, likely due to elevated wind-driven mixing from stronger winds. The variability of WW observed is tied to various mechanisms that impact upper ocean structure, such as varying eddy kinetic energy (Dove et al., 2022; Nikurashin et al., 2013), differing wind stress fields (Abernathey et al., 2011; Lin et al., 2018), and CDW outcropping pathways (Narayanan et al., 2023; Tamsitt et al., 2021).

In this study we provide revised criteria for defining the vertical distribution of WW. We apply this to 18 years of in-situ observations over the SO to examine the spatiotemporal distribution of WW, its properties using seasonal climatologies and the dynamics governing these distributions. A seasonally evolving heat budget for WW is estimated to shed light on the dominating processes which impact the evolution and erosion of WW and to better understand its connection to the surface layer of the ocean and meridional circulation. Finally, we reveal linkages between WW distribution and its properties to the underlying topography of the SO. WW variability is directly tied to rates of overturning, so determining possible pathways of enhanced overturning is critically important in understanding our global climate and the redistribution of oceanic properties.

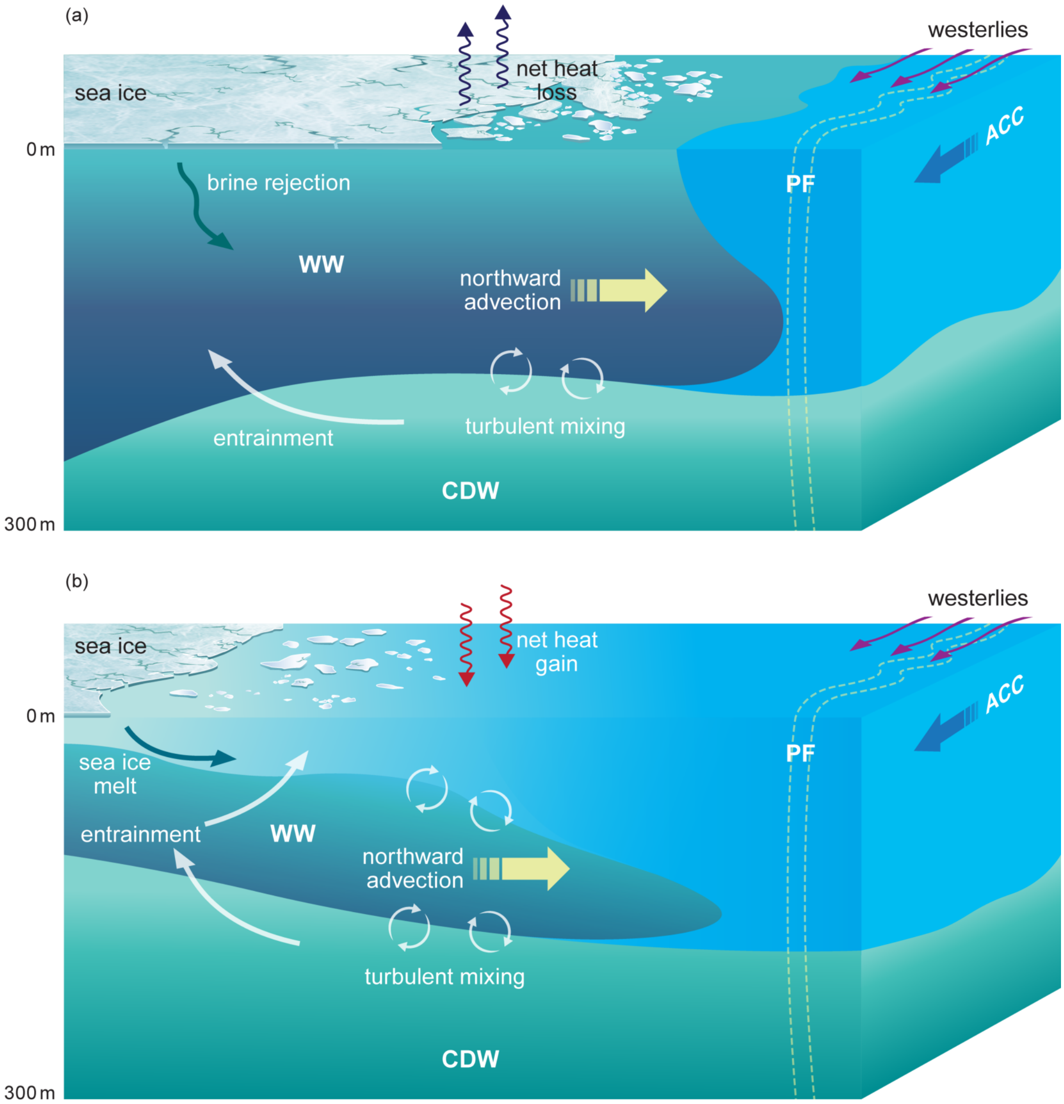


**Figure 1. Conceptual view of Antarctic Winter Water.** (a) $WW_{ML}$ in wintertime and (b) $WW_{SS}$ in summertime following summertime mixed layer restratification. Shown are the various physical mechanisms that impact the formation, distribution and erosion of WW.

# 2 Data and Methods

## 2.1 Hydrographic Profiles

This study uses hydrographical profiles south of 40°S from the period 2004 to 2021 compiled using the Argo float dataset (Wong et al., 2020), tagged marine seals dataset (MEOP: Marine Mammals Exploring the Oceans Pole to Pole) (Treasure et al., 2017), Southern Ocean biogeochemical floats (SOCCOM: Southern Ocean Carbon and Climate Observations and Modeling) (SOCCOM, 2019), as well as ship-based CTD casts and glider profiles (from WOD18: The World Ocean Database 2018) (Boyer et al., 2018). Data are relatively well distributed across the SO due to sampling from the Argo and MEOP programmes (Figures 2e-2h), which is extensive compared to limited historical CTD ship-based data collection (Brett et al., 2020). The Pacific sector is mainly sampled throughout the annual cycle via the Argo programme, whereas MEOP data cover a great extent south of the Polar Front, particularly in the Atlantic and Indian Ocean sectors, as well as below sea ice and across the circumpolar continental shelf (Narayanan et al., 2023). MEOP seals are tagged in the summertime, so provide least coverage in spring after CTD sensors have dropped off the seals from molting their winter fur, whilst their habitat location and foraging behavior largely dictate their spatial distribution (McMahon et al., 2019).

Additionally, the location of float sampling is initially spatially biased to deployment location due to ship-based deployments, and subsequently follow quasi-Lagrangian trajectories. Therefore, float data are heterogeneously distributed in space and time (Figures 2a-2d) with different regions sampled in different time periods. There are fewer total profiles per month from 2020 and onwards (Figure 2i) because of limited scientific cruises during the global pandemic (Boyer et al., 2023; Sarmiento et al., 2023). Consequently, there are limited MEOP data in 2020 and 2021, but the remaining operating floats continued to sample the SO.

In sea-ice-covered regions, ship-based and seal-based measurements are geographically accurate as they contain GPS fixes; profiling floats, however, use a temperature-based sea ice avoidance algorithm and cannot transmit their location when under sea ice. Profiling floats park at depth when not profiling where the currents are assumed to be low, so the profile locations are linearly interpolated. For this study, we take it as appropriate for use since we are interested in broadscale findings, where the positional errors from linear interpolation have little effect when gridding to spatial bins of 1°, as shown by Wong and Riser (2011) who find a mean distance between profiles to be 32 km.

Float-based measurements of temperature and salinity have been corrected for any sensor biases in real-time and undergo delayed mode quality control testing (Wong et al., 2020). We only use data flagged as "good" and "under sea-ice" for all data sources. Following Wilson et al. (2019), we further quality control the data such that each profile contains at least five measurements in the top 300 dbar with at least one data point in the top 25 dbar to ensure representation of the upper ocean processes of interest, ensuring both the ML and majority of WW properties are captured. Profiles containing unrealistic values of potential temperature and practical salinity are removed such that $-2.5 < T < 16$ °C and $30 < S < 36$. These thresholds are obtained from the observed range of properties south of the Subantarctic Front. Consequently, in this study, we analyze 620,293 quality-controlled CTD profiles.

The profiles are linearly interpolated to a standard two dbar vertical grid followed by a one-dimensional Gaussian filter with a standard deviation of four to smooth the data but retain key features. Absolute salinity and conservative temperature are derived from these gridded, quality controlled and smoothed profiles. The WW detection algorithm (Section 2.2) is applied to each profile, with all depth-related variables converted to meters, before gridding the data onto a median 1°×1° latitude-longitude seasonal climatol-

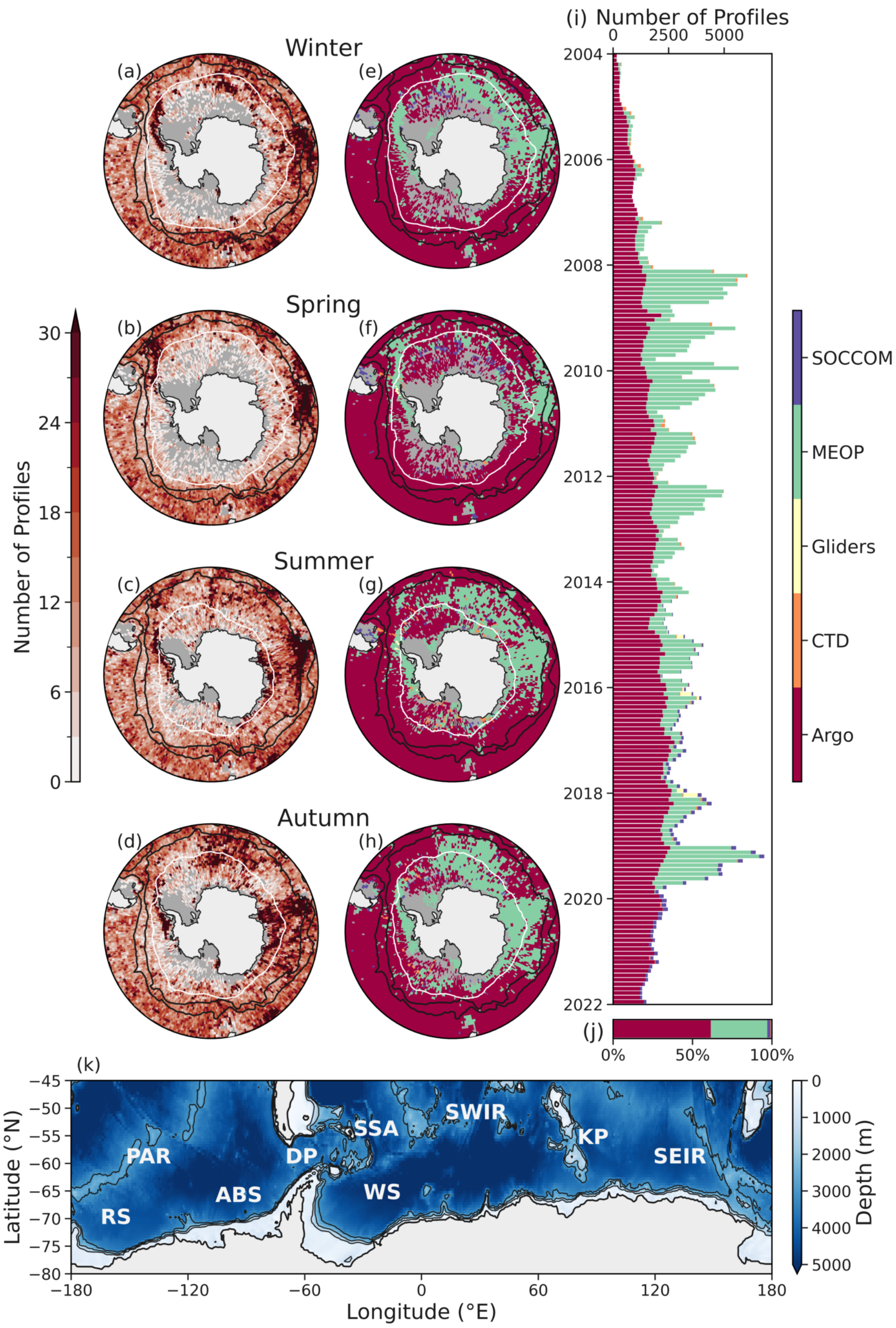


**Figure 2. Hydrographic data distributions**. (a-d) Spatial distribution of the total number of hydrographic profiles per season from winter through to autumn, respectively. (e-h) Spatial distribution of the mode data source per grid cell. The black contours indicate the Polar Front and Subantarctic Front, and the white lines are the mean 15% sea ice concentration for the relevant season in (a-h). (i) Monthly time series of data sources (stacked) across the Southern Ocean. (j) Total proportion of data per data source as a percentage. (k) Southern Ocean bathymetry map with bathymetric features and seas. Thin black lines denote 1, 2 and 3 km bathymetric contours. Abbreviations are as follows: RS=Ross Sea, PAR=Pacific-Antarctic Ridge, ABS=Amundsen and Bellingshausen Seas, DP=Drake Passage, SSA=South Sandwich Arch, WS=Weddell Sea, SWIR=Southwest Indian Ridge, KP=Kerguelen Plateau, SEIR=Southeast Indian Ridge.

ogy. Since the formation and annual cycle of WW is tied to sea ice evolution, we define the climatological seasons based on the annual cycle of sea ice formation and melt such that January, February, and March represent summer, and so on (Holland, 2014; Goosse et al., 2023).

### 2.2 Antarctic Winter Water Algorithm

WW definitions vary in present literature. Park, Charriaud, Pino, and Jeandel (1998) define WW as a relatively homogenous subsurface layer south of the PF with a subsurface temperature minimum, defining the upper boundary with a strong hydrographic gradient (thermo-, halo-, pycnocline) and the lower boundary as strong temperature and salinity gradients. Evans et al. (2018) define WW via a temperature threshold such that $\Theta < 0.5$. Sabu et al. (2020) define WW as the depth of the coldest temperature inversion observed below the ML. Giddy et al. (2023) use a more comprehensive definition: the upper boundary as the mixed layer depth (MLD), core depth as the temperature minimum below the MLD, and lower boundary as the max temperature gradient below the WW core, marking the boundary between WW and CDW.

We characterize WW into two classifications: mixed layer WW ($WW_{ML}$, Figures 1a and 3e) and subsurface WW ($WW_{SS}$, Figures 1b and 3f-3h). $WW_{ML}$ is defined as constrained to mixed layer (ML), taking the upper bound as the ML reference depth and the lower bound as the mixed layer depth (MLD); we assume the ML is well-mixed, and therefore take the mid-depth of MLD as the WW core depth, whilst the core properties are defined as the mean properties across the ML. $WW_{SS}$ only exists if there is a temperature inversion below the ML. That is, $WW_{SS}$ only exists if there are at least 10 inversions, equivalent to 20 m, between the mean ML temperature and subsurface temperatures. We describe $WW_{SS}$ through its core properties (the temperature minimum, the depth at which the temperature minimum occurs, as well as the salinity and density at that depth) and thickness (difference in depth between upper and lower boundary). We summarize the property definitions of the WW classifications in Table 1. Note that we define the MLD following the density difference criterion of 0.03 kg $m^{-3}$ from a reference density taken from the surface at 10 dbar, as per de Boyer Montégut (2004).

WW only exists if the core temperature is below 2 °C since this temperature denotes the boundary for the PF at 200 m depth (Belkin & Gordon, 1996; Morrow et al., 2008; Pollard et al., 2002). The PF is a baroclinic barrier to WW, marking the transition from beta- to alpha-dominating regimes in the upper ocean, which determines the existence of temperature inversions (Orsi et al., 1995; Stewart & Haine, 2016; Caneill et al., 2023). If the temperature at the lower bound is warmer than 2 °C, the 2 °C isotherm depth is used as the WW lower boundary instead. Further, if the core depth is deeper than the lower bound depth, we conclude no WW exists in that profile. Similarly, if the core temperature is warmer than 2 °C then we conclude no WW exists in that profile. The lower boundary and, or core depth of WW can feasibly reach depths below 300 m, for example via deep convection cells as a result of polynya driven processes, which typically are found close to the Antarctic continent (Morales Maqueda et al., 2004; Tamura et al., 2008; Mohrmann et al., 2021; Whitworth et al., 1994). However, these processes are associated with deep water formation (Jacobs, 2004; Johnson, 2008; Kusahara et al., 2017; Meredith, 2013), and therefore associated with dynamics outside the scope of this study. WW is otherwise typically found in the bounds of 50-200 m (Lund et al., 2021; Sabu et al., 2020) (Figure 3). Hence, WW profiles with a lower boundary deeper than 300 m are removed.

In total, 43% of all profiles (266,856 profiles) contain WW: 105,588 $WW_{ML}$ profiles and 161,268 $WW_{SS}$ profiles (Figures 3a-3d). We then compute the climatologies, which are smoothed using a 3°×3° latitude-longitude rolling mean and interpolated across a maximum gap of three missing grid cells to the maximum WW extent.

**Table 1. Summary of Antarctic Winter Water properties:** upper boundary, core and lower boundary depth definitions. We take depth, z to be positive and therefore increasing with depth.

| **Property** | $\mathbf{WW_{ML}}$ | $\mathbf{WW_{SS}}$ |
|---|---|---|
| Upper boundary ($z_{ub}$) | 10 m | MLD or 2°C isotherm if $T_{MLD}$ >2°C |
| Core | Core depth: mid-depth of ML<br>Core T, S, density: average across ML | Depth of temperature minimum such that<br>$z_{ub}<z_{core}<z_{lb}$ and $T_{min}<2°C$ |
| Lower boundary ($z_{lb}$) | MLD | $z_{core}<z(\frac{dT}{dz}_{max})<300$ dbar<br>or 2°C isotherm if $T_{core} > 2°C$ such that $z_{core}<300$ dbar |

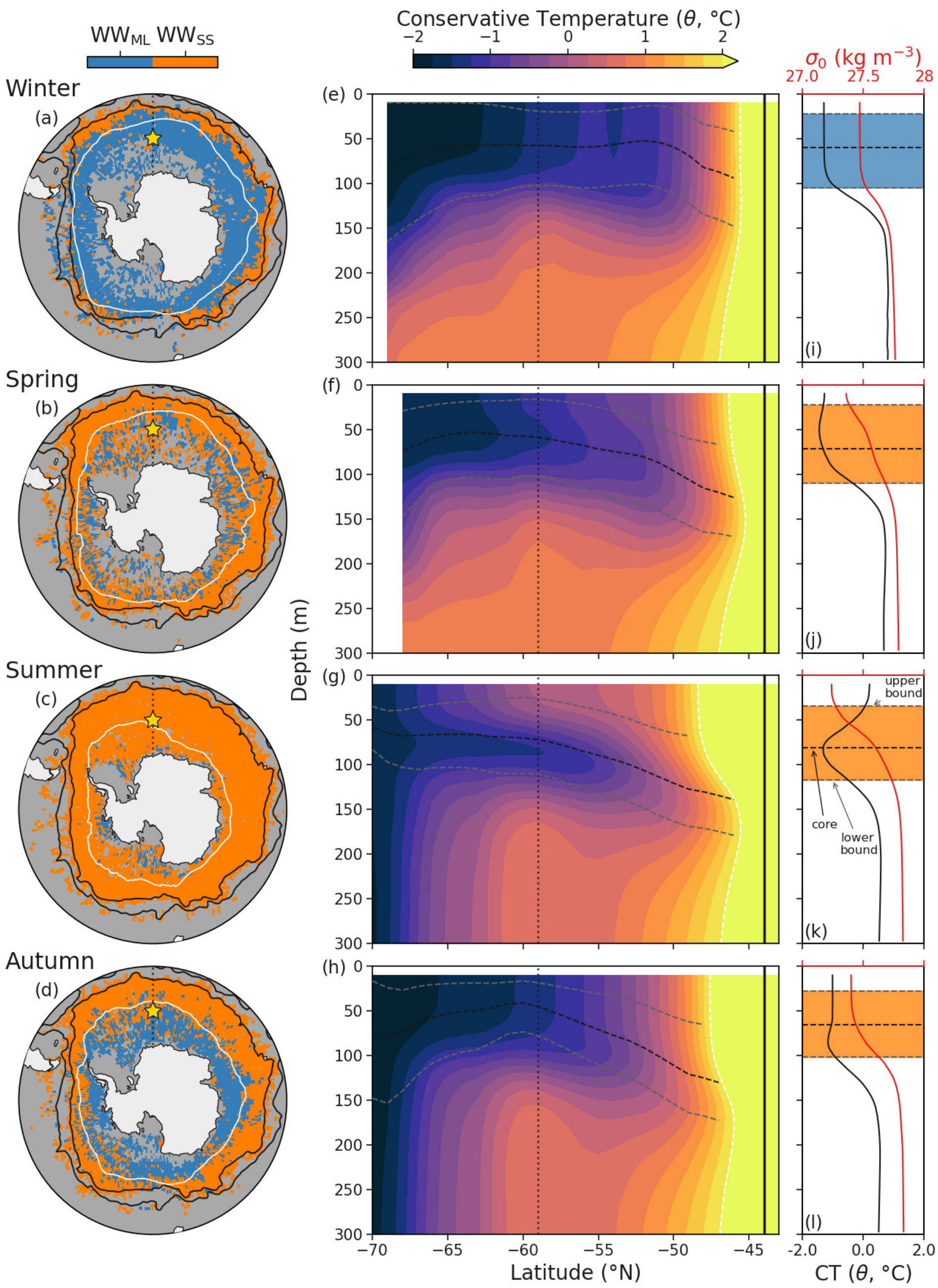


**Figure 3. Antarctic Winter Water classification.** (a-d) Spatial distribution of the mode classification of WW for each grid cell from winter through to autumn, respectively, where blue (orange) represents $WW_{ML}$ ($WW_{SS}$) profiles. The black lines denote the PF and SAF of the ACC, and the white lines show the seasonal mean 15% sea ice concentration; the dotted black line shows the cross section location in (e-h) and the star denotes the profiles in (i-l). (e-h) Smoothed meridional cross section along 0°E for each season. The solid black vertical lines denote the PF; the light gray dashed lines denote the upper and lower bounds of WW, the black dashed line denotes the WW core, and the white dashed line denotes the 2 °C isotherm. The dotted black lines show the location of the star in (a-d) and are the profiles shown in (i-l). (i-l) show profiles of conservative temperature (black) and potential density (red) from the location 59°S, 0°E throughout the seasonal cycle. The light gray dashed lines denote the upper and lower bounds of WW, and the black dashed line denotes the WW core as in (e-h). The classification is shown by shading: blue (orange) shading represents $WW_{ML}$ ($WW_{SS}$) profiles, as in (a-d).

### 2.3 Temperature Tendency / Heat Budget

Adapting the temperature tendency equation of Giddy et al. (2023) to Equation 1, we compute a temperature tendency of $WW_{SS}$ to investigate the dynamics that impact how WW evolves and erodes over the annual cycle to better understand the connection between the subpolar surface ocean and the meridional circulation system.

$$\overbrace{\frac{\delta T_{WW}}{\delta t}}^{(I)} = \frac{1}{\rho_0 C_p h_{WW}} \Bigg( \overbrace{\Delta Q_{SW}}^{\text{(II)}} + \overbrace{Q_{mixing}}^{\text{(III)}} + \overbrace{Q_{entrainment}}^{\text{(IV)}} + \underbrace{Q_{formation/erosion}}_{\text{(V)}} + \underbrace{Q_{residual}}_{\text{(VI)}} \Bigg). \quad (1)$$

Term (I) is the temperature tendency of the $WW_{SS}$ system, which can be calculated by taking the time derivative of the WW integrated heat content, $\frac{\delta T_{WW}}{\delta t} = \frac{\delta}{\delta t}\left(\frac{1}{h_{WW}}\int \text{thickness}\Theta\delta z\right)$ (Huguenin et al., 2022), after adjusting Θ by the freezing point of seawater to negate sign errors.

Term (II) represents the penetrative shortwave radiation absorbed by the WW layer, which is the difference in shortwave entering at the upper boundary and leaving at the lower boundary. This term is approximated via exponential decay of shortwave solar radiation from the surface using Jerlov water type II as per Paulson and Simpson (1977):

$$R_s(z) = R_s(0)\,[0.77\exp(\frac{-|z|}{1.4})+0.23\exp(\frac{-|z|}{14})]\,.$$

Term (III) is the down-gradient turbulent heat flux term across the ML-WW interface due to wind-driven mechanical mixing. Nicholson et al. (2022) show a close correlation between theoretical and observed dissipation rates in Southern Ocean summertime ($r^2 = 0.75$, see their Figure S5 in Supporting Information). Hence, we calculate the diffusivity, $\kappa$, such that:

$$\kappa = \Gamma\frac{\varepsilon}{N^2}$$

where the mixing coefficient is a constant, which we take as the modified Osborn number for a transitional regime, $\Gamma = 0.2$ (Osborn, 1980; Bouffard & Boegman, 2013; Gregg et al., 2018). Assuming winds is the dominant driving factor, we approximate turbulence dissipation, ($\varepsilon$) at the base of the mixed layer (i.e., the upper boundary of the WW) via law of the wall (von Kármán, 1931) such that $\varepsilon = \frac{u_*^3}{kz}$, using frictional velocity, $u_*^3 = \sqrt{\frac{\tau}{\rho_{\text{sw}}}}$, where $\tau$ is the climatological mean wind stress and $\rho_{\text{sw}} = 1035$ kg m$^{-3}$ is the reference density of seawater (Huguenin et al., 2022). Further, we use von Kármán's constant, $k = 0.41$, and z as the MLD. $N^2$ is the stratification across the upper boundary of the $WW_{SS}$.

Term (IV) measures the change in WW heat from entrainment and detrainment, which results in a flux of temperature, at both the upper (ML-WW) and lower (WW-CDW) boundaries. Term (IV) is calculated using the general formula, $Q_{\text{ent}} = \frac{H}{h} w_{e_{IF}} \Delta T_{IF}$, where H is the Heaviside function of vertical velocities such that

$$H\left(w_{e_{IF}}\right) = \begin{cases} 0 & \text{if } w_{e_{IF}} < 0, \\ 1 & \text{if } w_{e_{IF}} > 0. \end{cases}$$

where $w_{e_{IF}} = \frac{dh}{dt}$ is the vertical velocity and $IF$ is the interface between water masses. $\Delta T$ is taken across the ML-WW interface as the difference between the ML temperature and 15 m below the MLD (Pellichero et al., 2017; du Plessis et al., 2022). Across the WW-CDW layer, we use the average WW temperature minus the temperature 5 m below the WW, as per Giddy et al. (2023).

Term (V) represents temperature due to the formation or erosion of $\mathrm{WW_{SS}}$. $\mathrm{WW_{SS}}$ is created following the restratification of the wintertime ML, resulting in a warm and fresh summertime ML that caps a cold layer of remnant wintertime ML that we have defined as $\mathrm{WW_{SS}}$. $\mathrm{WW_{SS}}$ is formed if there exists no $\mathrm{WW_{SS}}$ in $t_{i-1}$ and $\mathrm{WW_{SS}}$ exists in $t_i$, which results in an input of heat into the $\mathrm{WW_{SS}}$ system, thereby warming $\mathrm{WW_{SS}}$. Conversely, we assume $\mathrm{WW_{SS}}$ has been eroded if there is $\mathrm{WW_{SS}}$ in $t_{i-1}$ and no $\mathrm{WW_{SS}}$ in $t_i$, which causes a cooling of $\mathrm{WW_{SS}}$. This assumes that $\mathrm{WW_{SS}}$ totally erodes over the annual cycle and that $\mathrm{WW_{ML}}$ formation includes remaining $\mathrm{WW_{SS}}$ re-entrained into the wintertime ML. However, given the temporal resolution of the seasonal climatology, it does not allow for direct observation of total erosion $\mathrm{WW_{SS}}$.

Lastly, term (VI) incorporates any processes not accounted for in the other terms, which includes (but is not limited to) background mixing, diffusive convection, small-scale processes, uncertainties in the calculated terms, and horizontal advection term. Diffusive staircases perpetuate across large regions of the SO (van der Boog et al., 2021). Whilst the resultant diffusive mixing is important for water mass transformation (Evans et al., 2018), the heat flux contribution remains small (Bebieva & Speer, 2019; Giddy et al., 2023; Wilson et al., 2019). Further, vertical processes, such as submesoscale motions, are not resolvable given the geostrophic scale of the gridded dataset, meaning their attributed heat fluxes are not directly computable (Section 4.2), but are incorporated as part of the geostrophic mean field flux. Given the numerical findings of Morrison et al. (2016), who show a substantial northward heat flux by the mean flow, we therefore assume that lateral advection dominates the residual term, similar to Pellichero et al. (2018).

### 2.4 Other Data

We determine the sea ice edge using gridded daily sea ice data (Spreen et al., 2008). Since WW evolution is tied to sea ice dynamics, we often distinguish the SO into two domains: the under-ice zone, which we define as the region south of the 15% sea ice concentration line for the respective period that is typically associated with sea ice cover, which includes a transitional region from an area of mixed sea ice and open ocean conditions to the sea ice capped ocean; and the open-ocean zone refers to north of the 15% sea ice concentration line, which is not necessarily ice-free but is an area of mixed sea ice conditions that transitions from the sea-ice capped ocean to open ocean.

ACC boundaries of the PF and SAF were defined using absolute dynamic topography at -0.58 m and -0.1 m, respectively (Park et al., 2019), using monthly altimetry data via AVISO. Shortwave radiative heat flux ($Q_{sw}$) and wind stress, $\tau$, at monthly and 1° resolution from ERA5 reanalysis of the European Centre for Medium Range Weather Forecasts (Hersbach et al., 2023) are used for the calculation of term (I) and term (III) of Equation 1, respectively, and are gridded before use in computation.

## 3 Results and Discussion

### 3.1 The Seasonal Cycle of Antarctic Winter Water

#### *3.1.1 Antarctic Winter Water Spatial Extent*

The annual cycle of WW is intricately linked to the sea ice cycle (Figure 3a-3d): WW forms during the sea ice formation periods of autumn and winter in the under-ice zone in the ML ($WW_{ML}$) as a cold and homogenous water mass (Figures 1a, 3a and 3d). $WW_{ML}$ also forms north of the 15% sea ice concentration line from ocean surface layer cooling. In winter, $WW_{ML}$ forms a mean maximum extent of 400 $\pm$ 280 km (approximately 3.4 $\pm$ 2.8 degrees of latitude) north of the sea ice concentration line in the open-ocean zone. 78% of WW profiles in winter are classified as $WW_{ML}$, and the remainder of profiles are $WW_{SS}$ (profiles containing a subsurface temperature minimum) in the open-ocean zone at the northern extent of WW. The $WW_{SS}$ profiles are on average north of the Southern Boundary of the ACC, as shown by Jones et al. (2023), which delineates regions of differing oceanic properties.

During periods of sea ice melt (spring and summer), the ML restratifies and warms from solar heating, which overlays the remnant cold ML. Consequently, there exists a subsurface temperature minimum, $WW_{SS}$ (Figures 1b, 3f-h and 3j-l ), which is sustained via beta ocean properties (Stewart & Haine, 2016). The spring season has a heterogeneous mix of $WW_{ML}$ and $WW_{SS}$ classified profiles, with 76% of spring WW profiles being $WW_{SS}$ (Figure 3b). The $WW_{ML}$ extent retreats at different rates around the circumpolar SO during spring; across and to the west of KP remains as a mix of $WW_{ML}$ and $WW_{SS}$ in the open-ocean zone, whereas the rest of the open-ocean zone is largely $WW_{SS}$.

The ocean transitions to a summer ocean that is dominated by $WW_{SS}$ (93% of WW profiles; Figure 3c). $WW_{ML}$ is only found near the Antarctic continent in summer, which are likely regions that do not form any $WW_{SS}$ throughout the entire annual cycle. An example of such a region is Pine Island Bay in the Amundsen and Bellingshausen Seas (ABS), where coastal modified CDW maintains a warm subsurface ocean and the Thwaites glacier concurrently drives a cold surface layer (Dotto et al., 2022). Similarly, $WW_{SS}$ persists throughout the entire annual cycle at the northernmost extent of WW domain (Figures 3a-3d and S1), which can only be sustained through cold subsurface WW being transported northward to the regions where $WW_{ML}$ do not form.

Surface ocean cooling and sea ice growth during autumn lead to an increase of $WW_{ML}$ (Figure 3d), with the under-ice zone almost totally $WW_{ML}$ and localized regions forming $WW_{ML}$ north of the 15% sea ice concentration line. Northern portions of the under-ice zone in the Weddell Sea and Ross Sea have a mix of $WW_{ML}$ and $WW_{SS}$, which is likely related to gyre circulation: cold WWs in the ML are maintained in the gyre core and edge, whilst mixing drives warmer and deeper (subsurface) WWs at gyre peripheries where the ocean transitions to ACC dynamics (Jones et al., 2023). Similarly, the northern under-ice region of the ABS has a mixed WW composition of $WW_{ML}$ and $WW_{SS}$.

WW profiles are largely constrained to the extent of the PF, as per the WW definition (Section 2.2; Table 1), but there are regions with WW detected northward of the PF. In the Pacific sector of the SO, WW is consistently detected north of the PF throughout the seasonal cycle (Figures 3a-3d); SAMW, similar to WW, forms via buoyancy loss and drives ML deepening, which takes place in the vicinity of the ACC and northwards (Boland et al., 2021; Cerovečki et al., 2013; Meijers et al., 2019; Wang et al., 2022). Hence, the detection of WW north of the PF in the Pacific sector where Shallow Salinity Minimum Water (Karstensen, 2004) is observed in a region transitioning from a beta density regime to an alpha density regime (Roquet et al., 2022) (see their Figure 2b). Therefore, WW may potentially be aliased with the cold Subantarctic Mode Water of the Pacific sector, which is also a low stratification water mass formed through surface buoyancy loss in the ML (Li et al., 2021; Herraiz-Borreguero & Rintoul, 2011; Xia et al., 2022). These WW profiles are removed from the analysis. Further, there is likely very little WW identified between the PF and SAF due to the ACC acting as a strong baroclinic barrier.

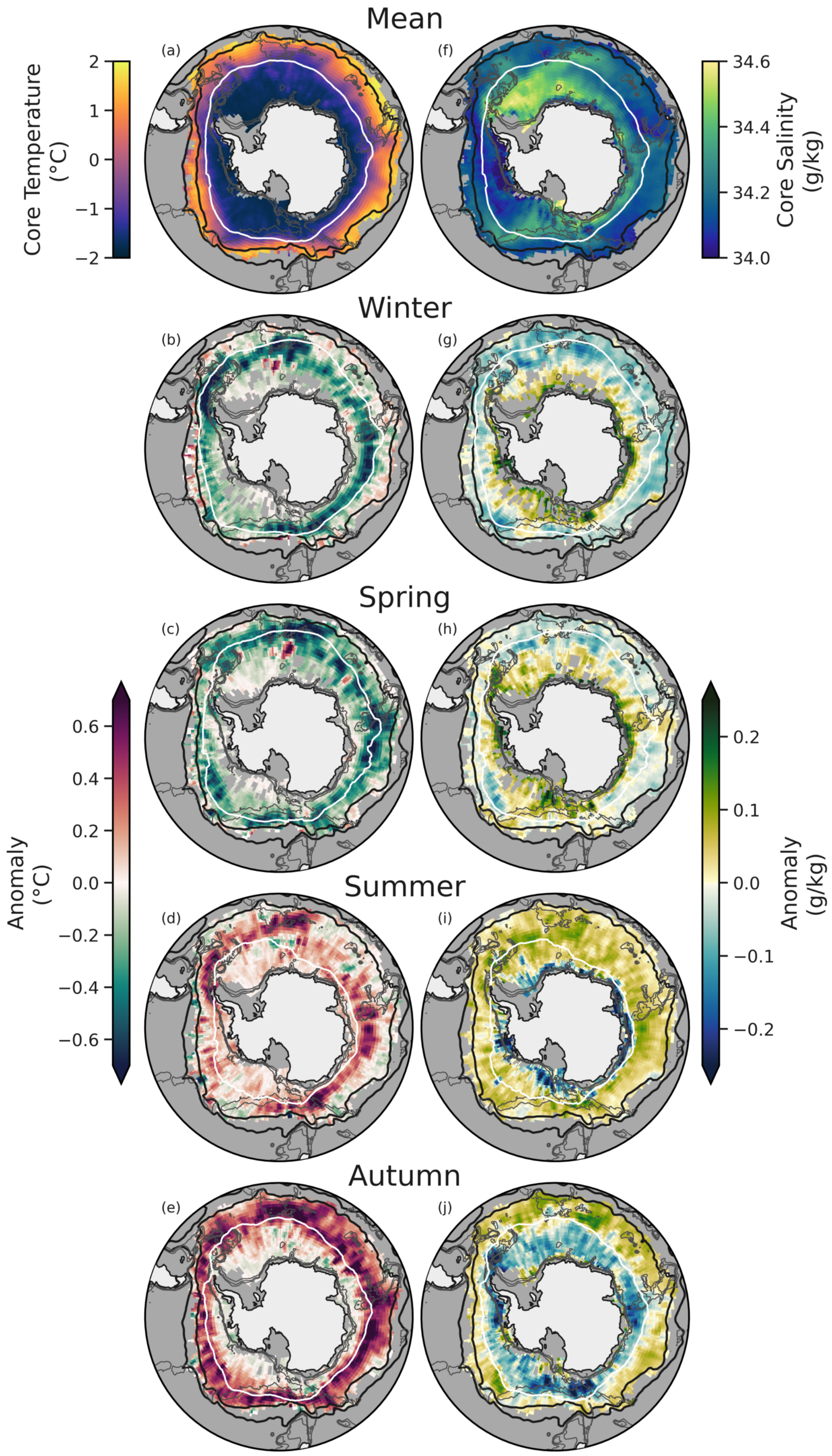


**Figure 4. Annual mean and seasonal anomalies of Antarctic Winter Water:** (a-e) core conservative temperature, and (f-j) core absolute salinity. A negative (positive) anomaly implies a decrease (increase) from the annual mean. Black lines indicate the PF and SAF, white lines indicate the mean 15% sea ice concentration for the time period, and gray lines indicate 1km, 2km and 3km isobaths.

#### *3.1.2 Antarctic Winter Water Core Thermohaline Properties*

Core temperature and salinity of WW exhibit distinct seasonal cycles (Figures 4); nonetheless, both core properties exhibit large-scale spatial homogeneity in the under-ice and open-ocean zones (Figures 4a, 4f, 5b and 5d). WW forms below sea ice from a cold ocean nearing freezing point, so is largely homogenous in its mean temperature across the SO (Figures 5a), particularly in the under-ice zone (Figures 4a and 5b). Brine rejection from sea ice formation, and surface cooling drives buoyancy loss that results in a deepening of the ML (Wilson et al., 2019). Consequently, the coldest and saltiest WW is consistently observed during under-ice conditions throughout the annual cycle (Figures 4a, 4f, 5b and 5d).

Spatially, WW core temperature in the under-ice zone remains largely homogeneous with a mean temperature of -1.4 ± 0.5°C in the under-ice zone, whilst core salinity exhibits a circumpolar mean of 34.26 ± 0.18 g/kg (Figures 5b and 5d). WW cores are substantially fresher (34.11 ± 0.12 g/kg) in the Amundsen-Bellingshausen Seas (ABS): the proximity of the ACC fronts and the eastward limb of the Ross Gyre transport CDW southwards, maintaining the region as a warm shelf sea and facilitating elevated sea ice melt rates, which is likely responsible for the fresher WW core salinity as well as freshening the under-ice zone mean and increasing the standard deviation (Figure 5c) (Nakayama et al., 2018; Narayanan et al., 2023; Tamsitt et al., 2021; Thompson et al., 2018). The coldest and most saline WW cores are observed within the polar gyres (approximately -1.5 °C, 34.6 g/kg; Figures 4a, 4f, 5a and 5c), which are maintained through their southern proximity and elevated sea ice production. On the other hand, there is distinct variability displayed in all core properties (Figures 4-7) in the open-ocean zone when comparing properties up- and downstream of large topographic features. Our findings agree with Sabu et al. (2020), who show distinctly warmer core temperatures downstream of Kerguelen Plateau (KP); similar distinctions can be made when considering the differences in core properties up- and downstream of the Southwest Indian Ridge (SWIR) and the Southeast Indian Ridge (SEIR). These differences in properties may be a consequence of topographic features stirring the downstream water column, which enhances mixing rates (Nikurashin et al., 2013; Rosso et al., 2015; Mashayek et al., 2017; Tamsitt et al., 2017) and alters the spatial gradients of WW core temperature and salinity. Nonetheless, meridional mean WW core temperatures (Figure 5a) do not differ substantially across the circumpolar SO since the formation of the temperature minimum is determined during WW formation in $\mathrm{WW_{ML}}$ from wintertime net ocean heat loss, and consistently approaches freezing point (Figures 4b-4e and 5a).

Core temperature and salinity in the open-ocean zone have a strong tie to latitudinal extent, getting warmer and fresher as latitudes extend northward with a mean warming rate of 0.16 °C per degree of latitude and decreasing in salinity at a rate of 0.01 g/kg per degree of latitude in the open-ocean zone (Figures 5b and 5d). Note that the latitudinal mean core salinity peaks in freshness with a large standard deviation at approximately 70°S (34.19 ± 0.22 g/kg; Figure 5d); this is influenced by the fresh WW core salinities in the ABS, which is the only region that has a meridional mean salinity below 34.2 g/kg (Figure 5c). The mean open-ocean zone core temperature and salinity are 0.6 ± 0.8 °C and 34.23 ± 0.10 g/kg, respectively, with the warmest and freshest cores found in the northernmost domain of WW extent (∼50°S; Figures 5b and 5d). WW core temperature and salinity properties that are typically associated with under-ice conditions (i.e. colder, more saline) extend northwards into the open-ocean zone in regions that align with large topographic features; that is: Pacific-Antarctic Ridge (PAR), South Sandwich Arch (SSA), SWIR, KP and the SEIR (Figures 4a, 4f, 5a, and 5c). This agrees with the findings of Park et al. (2009), who observed a subsurface cold water tongue advected northwards across the KP.

WW core temperature exhibits large changes in temperature throughout the annual cycle, which are spatially heterogeneous (Figures 4b-4e). In winter, a net ocean-atmosphere

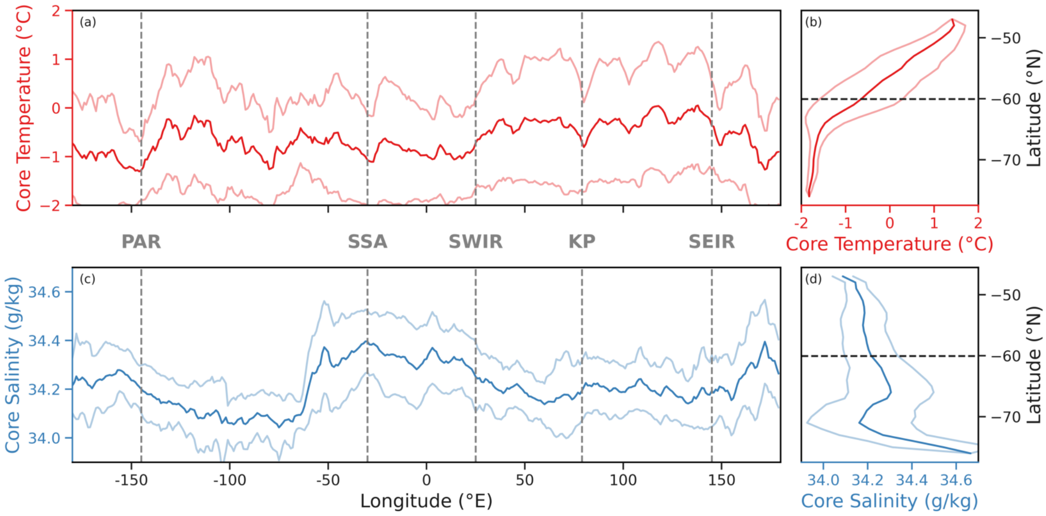


**Figure 5. Meridional and zonal means of Antarctic Winter Water core properties.** Meridional and standard deviation of (a) core temperature and (c) core salinity. Zonal mean and standard deviation of (b) core temperature and (d) core salinity. Dashed light gray vertical lines in (a) & (c) indicate locations of topographic features and are labeled as in Figure 2. Dashed black horizontal lines in (b) & (d) indicate the location of the mean 15% sea ice concentration.

heat loss cools the entire SO forming cold $WW_{ML}$ below sea ice (Figure 3a). WW displays the largest seasonal temperature anomaly in winter (-0.5 °C anomaly) close to the sea ice edge, where there is the greatest change in WW core temperature throughout the annual cycle. Further, large wintertime temperature anomalies are observed in the Weddell Sea and Indian Ocean sector. The largest anomalies align with or are downstream of topographic features. These regions have elevated mixing rates (Dove et al., 2022; Mashayek et al., 2017; Mohrmann et al., 2022) so have warmer summertime WW temperatures. This thereby skews the annual mean temperature, which results in a larger magnitude anomaly signal in wintertime. Therefore, the large magnitude anomaly regions in wintertime may be representative of regions with elevated mixing rates. The ABS exhibits a smaller magnitude of temperature anomaly (-0.3 °C anomaly) in winter. Similar low magnitude temperature anomalies are observed (but positive) in the ABS during the warming season in summer (Figure 4d).

WW core temperature is at its coldest mean seasonal state in spring at -0.7 ± 1.2 °C (Figure 4c). The sea ice begins to recede as the net heat flux becomes positive between September-October (Tamsitt et al., 2016), so the SO transitions to a $WW_{SS}$-dominated ocean (Figure 3b and 3c). Localized warming of WW cores initiates downstream of the Drake Passage (DP), as shown by the lower magnitude temperature anomaly (Figures 4c and S2c in Supporting Information). This region is highly energetic, resulting in a higher rate of mixing and, thus, a faster onset of warming due to mixing with subsurface CDW and the warm surface ML (Stephenson Jr. et al., 2012). Large-scale warming of the WW core follows in summer (Figure 4d and S2d), initiated in the Atlantic and Indian Ocean sectors downstream of topographic features: DP, SSA, KP, and PAR. In the regions of deeper bathymetry and fewer topographic features (such as west of KP and in the Pacific abyssal plain), mixing rates are lower and therefore warming of WW onsets in autumn, later in the seasonal cycle (Figure 4e) (Frants et al., 2013; Rosso et al., 2015; Waterhouse et al., 2014). WW across the SO in autumn is at its warmest mean core temperature at -0.5 ± 1.2 °C due to the erosion of $WW_{SS}$ in the open-ocean zone (Figure 4e).

Note that there is a localized patch in the eastern Weddell Sea that has a warm mean core temperature (59°S, 7°E, Figures 4b-4e) so appears warmer throughout the winter and spring (Figures 4b and 4c). This patch aligns with a region of thin sea ice in the Weddell Gyre associated with southward CDW penetration (Holland et al., 2014; Vernet et al., 2019).

WW core salinity (Figures 4g-4j) has a clear seasonal cycle: WW cores are fresher in winter with a seasonal mean of 34.22 ± 0.16 g/kg. In winter, the WW is largely classified as residing in the ML ($WW_{ML}$), which is observed as fresher than the mean core salinity since the ML is largely composed of the fresh remnant summertime ML. The southern section of the winter and spring under-ice zone has a large negative anomaly signal due to elevated sea ice formation driving brine rejection and salinification of $WW_{ML}$. Salinity increases from the Antarctic continent northward in springtime (Figures 4h and S2h in Supporting Information) to the most saline period of the annual cycle with a seasonal mean WW core salinity of 34.25 ± 0.16 g/kg. In summer, the circumpolar SO WW core salinity has a positive anomaly. This is driven by $WW_{SS}$ mixing with the underlying salty CDW, which necessarily densifies WW through cabbelling via salinification (Figure 4i) (Evans et al., 2018; Groeskamp et al., 2016; Jones et al., 2023), as well as a component of salinity redistribution via advection as shown by (Pellichero et al., 2018). Regions close to topographic features in summer have a greater magnitude in core salinity anomaly, for example across the KP and along the PAR, because mixing rates are elevated and thereby increase salinification through mixing with CDW. Further, the Weddell Gyre eastward limb has an elevated summertime core salinity anomaly due to mixing with southward intruding CDW (Vernet et al., 2019; Jones et al., 2023). Around the Antarctic coastline, sea ice melt continues into summer leading to the freshening of $WW_{ML}$ (anomaly of approximately -0.2 g/kg). These localized coastal regions return to a positive anomaly in autumn (Figures 4j and S2j) from an increase in salinity via sea ice formation, driving the formation of $WW_{ML}$ in the under-ice zone. The autumn under-ice zone otherwise experiences a mass freshening, which is indicative of the change from the salty and capped $WW_{SS}$ to the fresh remnant summertime ML becoming $WW_{ML}$. The greatest changes in core salinity anomaly in autumn are observed in the under-ice zone, along the ABS to downstream of DP, as well as along the SEIR, where there is a large change from salty $WW_{SS}$ via mixing with CDW to fresher $WW_{ML}$. In the open-ocean zone, no sea ice formation takes place and WW remains classified as $WW_{SS}$, so WW core salinity continues to increase.

#### *3.1.3 Antarctic Winter Water Core Depth and Thickness*

Over the circumpolar extent, WW has a mean core depth of 88 ± 42 m and a mean thickness of 99 ± 30 m (Figures 6a, 6f, 7a and 7c). The mean WW core depth is shallower under-ice, with a mean depth in the under-ice zone of 60 ± 21 m (Figure 7b). Similarly, the WW layer is thinner in the under-ice zone with a mean thickness of 87 ± 27 m (Figure 7d). Coastal polynya formation near the Antarctic continent results in deep WW cores and thick WW layers due to extreme heat loss and are also synonymous with more persistent $WW_{ML}$ conditions (Figures 3a-3d). Consequently, the standard deviation magnitudes of WW core depth and thickness are large for the under-ice zone, which is otherwise relatively spatially homogeneous (Figures 7b and 7d). Below sea ice submesoscale fluxes are heightened in the wintertime due to deeper mixed layers and stronger lateral gradients (Biddle & Swart, 2020). Because submesoscale fluxes are associated with enhanced vertical fluxes, which, in this region would transport warm and salty CDW water into the $WW_{ML}$, enhanced submesoscale fluxes in winter may contribute to maintaining a the observed consistent WW depth and thickness in the under-ice zone. WW core depth and thickness in the open-ocean zone have a mean of 127 ± 35m and 117 ±

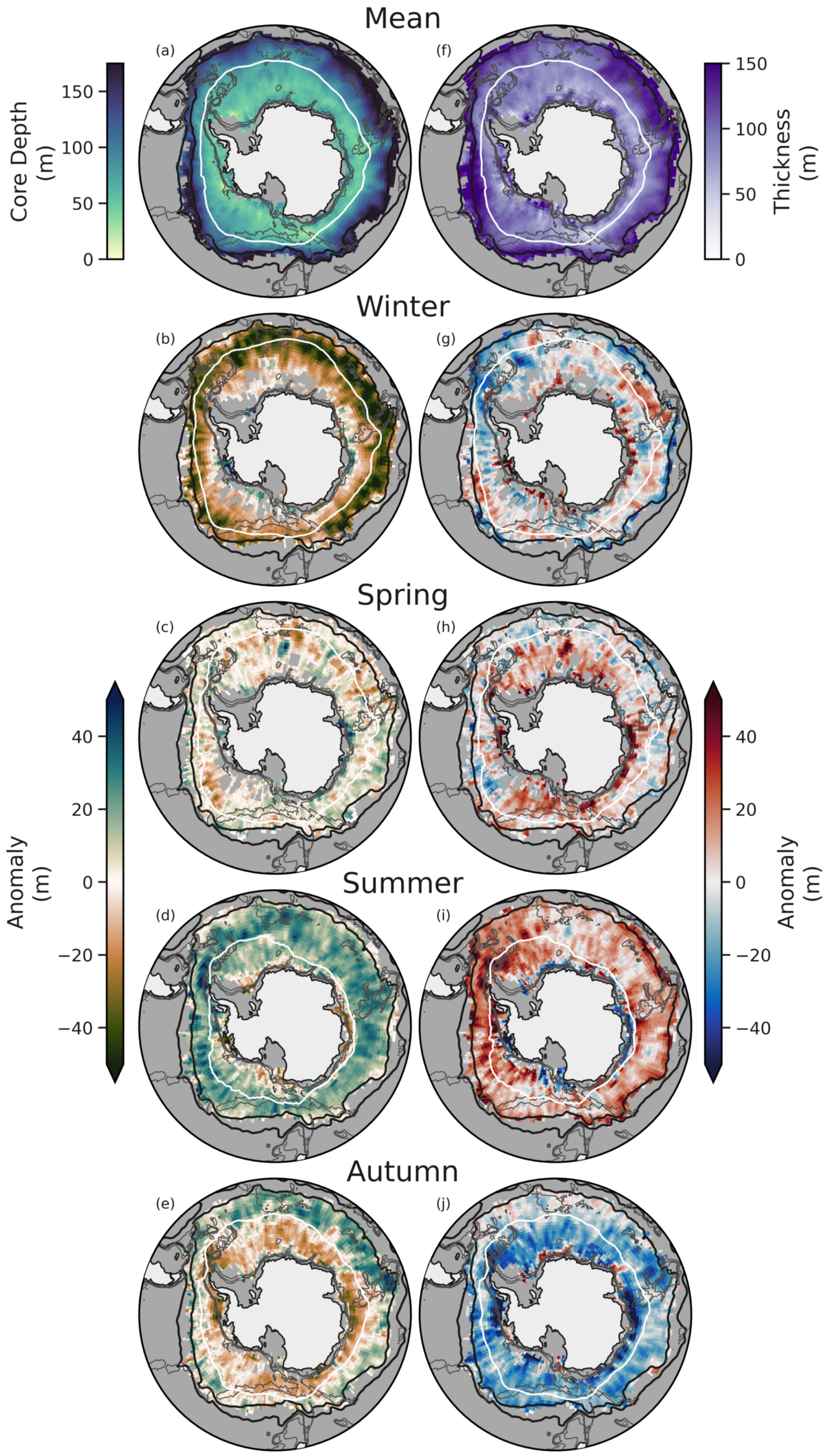


**Figure 6. Annual mean and seasonal anomalies of Antarctic Winter Water:** (a-e) core depth, and (f-j) thickness. (b-e) Core depth seasonal anomaly: positive (negative) indicates deeper (shallower) than the annual mean; (g-j) thickness anomaly: positive (negative) indicates thicker (thinner) than the annual mean. Black lines indicate the PF and SAF, white lines indicate the mean 15% sea ice concentration for the time period, and gray lines indicate 1km, 2km and 3km isobaths.

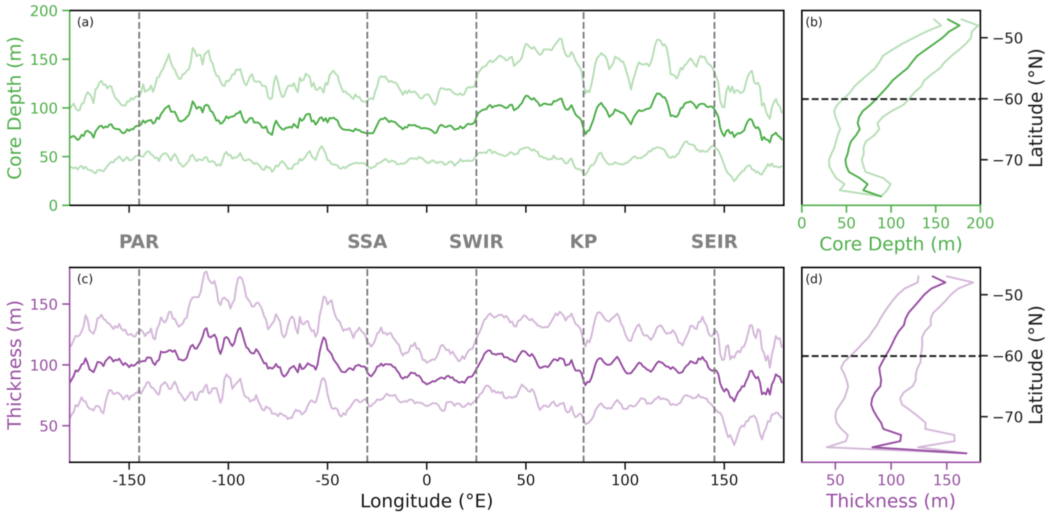


**Figure 7. Meridional and zonal means of Antarctic Winter Water core properties.** Meridional mean and standard deviation of (a) core depth (green) and (c) thickness (purple). Zonal mean and standard deviation of (b) core depth and (d) thickness. Dashed light gray vertical lines in (a) & (c) indicate locations of topographic features and are labeled as in Figure 2. Dashed black horizontal lines in (b) & (d) indicate the location of the mean 15% sea ice concentration.

25 m, respectively, and both have a northward latitudinal gradient in the open-ocean zone, with an average deepening rate of 6 m per degree of latitude northward and an average thickening rate of 3 m per degree of latitude northward. The deepest cores are found close to the PF (Figures 6a and 7b), whilst the thickest layer of WW are observed close to the Antarctic continent (Figures 6f and 7d). The average deepening and thickening of WW towards the north largely follows the deepening extent of CDW equatorward of the Antarctic shelf and can be associated with the reduced stratification and deep mixed layers associated with the PF region of the ACC (du Plessis et al., 2022). Other dominating patterns are shallower and thinner WWs near open ocean topographic features while under sea ice. These characteristics can be observed, for example, near the KP, SWIR, as well as in the Atlantic sector near the SSA and SEIR (Figures 6a, 6f, 7a and 7c). Deep and shallow MLs are observed up- and downstream of topographic features, respectively (Figures S3a-S3e), which directly impact WW thickness and core depth.

One potential explanation for up- and downstream discrepancies of WW thickness is that regions downstream of topographic features are greater in EKE (Dove et al., 2022; Rosso et al., 2014), which results in a heightened submesoscale field due to mesoscale strain via frontogenesis (McWilliams, 2021). This increases vertical mixing rates that act to increase MLD variance in space and time and alter the depth and thickness characteristics of WW (Viglione et al., 2018) from the initial stages of $WW_{ML}$, particularly in the presence of topographic features or in regions of heightened EKE in the ACC (e.g. at KP in Figure 6f). Since summertime MLs are ubiquitously shallow across the SO (mean summertime MLD is $41 \pm 18$ m) (Caneill et al., 2023; Dong et al., 2008; Pellichero et al., 2017), submesoscale ML restratification takes particular effect in winter when MLs are deep ($114 \pm 38$ m) leading to more 'patchy' spatial and temporal variability in MLD (Mahadevan & Campbell, 2002; du Plessis et al., 2017).

WW core depth (Figures 6b-6e) varies strongly seasonally (annual range of 88 m). In winter, the core depth is shallowest by definition because WW is largely classified as

$WW_{ML}$ (Figure 3a), with a seasonal circumpolar mean of 71 ± 34 m and the largest wintertime anomaly north of the sea ice edge where the core depth has shoaled (Figure 6b). Wintertime WW cores are only observed to deepen in the under-ice zone (Figure S2l), particularly close to the Antarctic shelf (e.g., Eastern Antarctica). Otherwise, wintertime core depth in the under-ice zone is relatively shallow and more spatially homogeneous with a seasonal under-ice zone mean of 55 ± 18 m, whereas the open-ocean zone is nearly double that with a mean winter core depth of 109 ± 33 m. Spring is a transition period from a $WW_{ML}$-dominated ocean to a $WW_{SS}$-dominated ocean (Figure 3b) as per our WW classifications (Table 1). As a result, the springtime SO is a heterogeneous mix of $WW_{ML}$ and $WW_{SS}$, particularly in the under-ice zone. Thus, the core depth deepens as $WW_{SS}$ becomes capped by the newly formed ML (Figures 6c and S2m) to a circumpolar mean of 93 ± 43 m. WW core depth continues to deepen in summer to the deepest seasonal mean of 100 ± 43 m, with a greater magnitude anomaly downstream of the DP and through the Weddell Gyre. In autumn, convection drives the formation of $WW_{ML}$ following sea ice formation (Figure 3d), mixing the remaining $WW_{SS}$ into the mixed layer and shoaling the WW core depth in the under-ice zone (Figure 6e). This shoaling leads to the largest discrepancy between mean core depth in the under-ice zone and open-ocean zone, which are 52 ± 22 m and 133 ± 38 m, respectively.

WW thickness displays patchiness in its seasonal cycle, thickening and thinning at different rates over the year (Figures 6g-6j and S2q-t). WW thickness in winter (Figure 6g) has a circumpolar mean of 100 ± 29 m, with a positive anomaly (thicker than the mean) close to the Antarctic continent where deep MLs form. WW is thicker close to the sea ice edge, such as in the Pacific and Indian sectors, which is driven by coastal polynya convective mixing processes. Furthermore, the low EKE upstream from the KP allows for the formation of thicker $WW_{ML}$. Downstream of the DP is a region of high EKE so $WW_{ML}$ remains thin. In spring, the SO begins to transition to a $WW_{SS}$ ocean and the mean circumpolar thickness increases to 108 ± 28 m.

Summer WW displays the thickest seasonal mean of 109 ± 33 m (Figure 6i). Thickening of $WW_{SS}$ is indicative of a deeper subsurface maximum temperature gradient, i.e. lower boundary (Figure S3n in Supporting Information), due to CDW mixing with $WW_{SS}$ which blurs the lower boundary. Close to the Antarctic continent, summertime WW thins due to elevated mixing along the Antarctic Slope Front through the WW layer, as shown by Hirano et al. (2010) in East Antarctica. Hirano et al. (2010) also computed an upward heat flux in East Antarctica that is more than double the upward heat fluxes observed in both the WS and western Peninsula shelf region (in ABS). Our results of an elevated magnitude of shallowing of the WW lower boundary depth along the coastline of the Indian sector (Figure S3n) agrees with these findings of increased heat fluxes. Further, WW is observed to reduce in thickness in the Ross Gyre in summer, which may be attributed to the seasonality in Ross gyre circulation, with a reduced summertime gyre strength driving increased heat flux from subsurface CDW (Dotto et al., 2018). A greater magnitude anomaly of summertime WW thickening is observed in the ABS and WS. These appear to thicken due deepening of the lower boundary (Figure S3n), which is a signal of WW mixing with underlying CDW resulting in the max temperature gradient (that is, the lower boundary; Table 1) observed at a deeper depth. This posit is supported by the core temperature increasing in summer (Figure 4d).

The seasonal mean WW thickness is observed at its thinnest in autumn with a mean of 81 ± 29 m (Figure 6j). Whilst WW close to the Antarctic continent is observed to thicken due to the formation of convective cells that contain $WW_{ML}$, WW otherwise thins in the under-ice zone due to the formation of $WW_{ML}$, mixing remaining $WW_{SS}$ with the ML (Figure 3d). In the open-ocean zone, WW remains as $WW_{SS}$ and erodes in thickness from continued mixing with underlying CDW as well as via deepening of the overlaying surface ML (Figure 3l, and Figures S3j and S3o).

#### *3.1.4 Seasonal Heat Budget of Antarctic Winter Water*

Given that temperature is the determining characteristic of the existence and classification of WW, we investigate a heat budget of $WW_{SS}$ following Equation 1 (Section 2.3) to understand the mechanisms driving the distribution of WW properties and to further examine the potential link in the overturning circulation system. The heat budget describes the integrated heat change across the WW layer normalized by WW thickness from season to season, which we decompose into its constituent terms (Equation 1; Section 2.3). Note, in this section we refer to the transition from autumn to winter as winter (first row in Figure 8), which represents autumn subtracted from winter, and so on.

There are several physical processes that may impact the $WW_{SS}$ heat budget (Figure 1), including penetrative shortwave radiation, vertical mixing, entrainment and detrainment, $WW_{SS}$ formation (via summertime restratification of the ML, capping the subsurface remnant wintertime ML) as well as $WW_{SS}$ erosion (via the onset of winter convection). $WW_{SS}$ formation and erosion is the emergence and disappearance of $WW_{SS}$ from one season to the next, and accounts for physical processes that may not be entirely captured by this dataset due its temporal coarseness. The former terms can be computed following Equation 1. The residual term consists of processes not accounted for by the other terms, such as diffusive convection, background mixing, and lateral advection (Section 2.3). We take advection to dominate the residual signal since diffusive and background mixing both make small contributions to heat fluxes (Bebieva & Speer, 2019; Giddy et al., 2023; van der Boog et al., 2021), whilst lateral advection is known to play a significant role in SO heat fluxes (Morrison et al., 2016).

The temperature tendency of $WW_{SS}$ (Figure 8) and its constituent terms (Figure S4 in Supporting Information) show clear seasonality. $WW_{SS}$ experiences an annual tendency to lose heat with an annual mean of -0.02 ± 1.67 °C season$^{-1}$ across the circumpolar SO. The largest mean cooling is observed in winter with a mean temperature tendency of -0.9 ± 1.80 °C season$^{-1}$ (Figure 8a), which is spatially heterogeneous. The greatest magnitude of wintertime cooling takes place downstream of the DP (-1.89 ± 1.12 °C season$^{-1}$), which is driven by the seasonal cycle of heat flux forcing, as shown by Stephenson Jr. et al. (2012). Conversely, spring has the largest mean warming of $WW_{SS}$, warming across the season 0.82 ± 2.17 °C season$^{-1}$ and greater warming rates observed in regions in close proximity to the PF. Summer continues to warm $WW_{SS}$ at a circumpolar mean rate of 0.54 ± 0.74 °C season$^{-1}$. du Plessis et al. (2022) observe WW warming by ∼1°C over the three months December through February at 60°S, 0°E with the largest changes in temperature observed across December and January (their Figure 7f), which agrees with our findings of greatest warming in spring (October to December) and continued warming in summer (January to March). In autumn, $WW_{SS}$ begins to cool again at a mean rate of -0.73 ± 1.39 °C season$^{-1}$, cooling at greater magnitudes southeast of KP, along the SEIR and in the DP.

The formation and erosion of $WW_{SS}$ is a leading order term of temperature tendency, accounting for ∼40% of the annual temperature tendency budget. $WW_{SS}$ formation represents the restratification of the ML in summertime to form a subsurface remnant wintertime ML. This addition of water and heat into the $WW_{SS}$ system thus appears as a warming of $WW_{SS}$ (red in Figures 8e-8h). Conversely, the erosion of $WW_{SS}$ results in the removal of heat from $WW_{SS}$ (blue in Figures 8e-8h), which can represent the erosion of $WW_{SS}$ or re-entrainment into the wintertime ML. During wintertime, 37% of WW profiles change from $WW_{SS}$ to $WW_{ML}$ resulting in the removal of heat from the $WW_{SS}$ system by a mean of -1.16 ± 0.79 °C season$^{-1}$, accounting for 61% of the seasonal temperature tendency. In spring, the surface ocean begins to warm such that 41% of $WW_{ML}$ profiles become (Figures 3 and S1b), resulting in a positive temperature tendency with a circumpolar mean of 0.87 ± 2.77 °C season$^{-1}$ and accounting for 54% of the season's temperature change. The minimum contribution (17%) from $WW_{SS}$ ero-

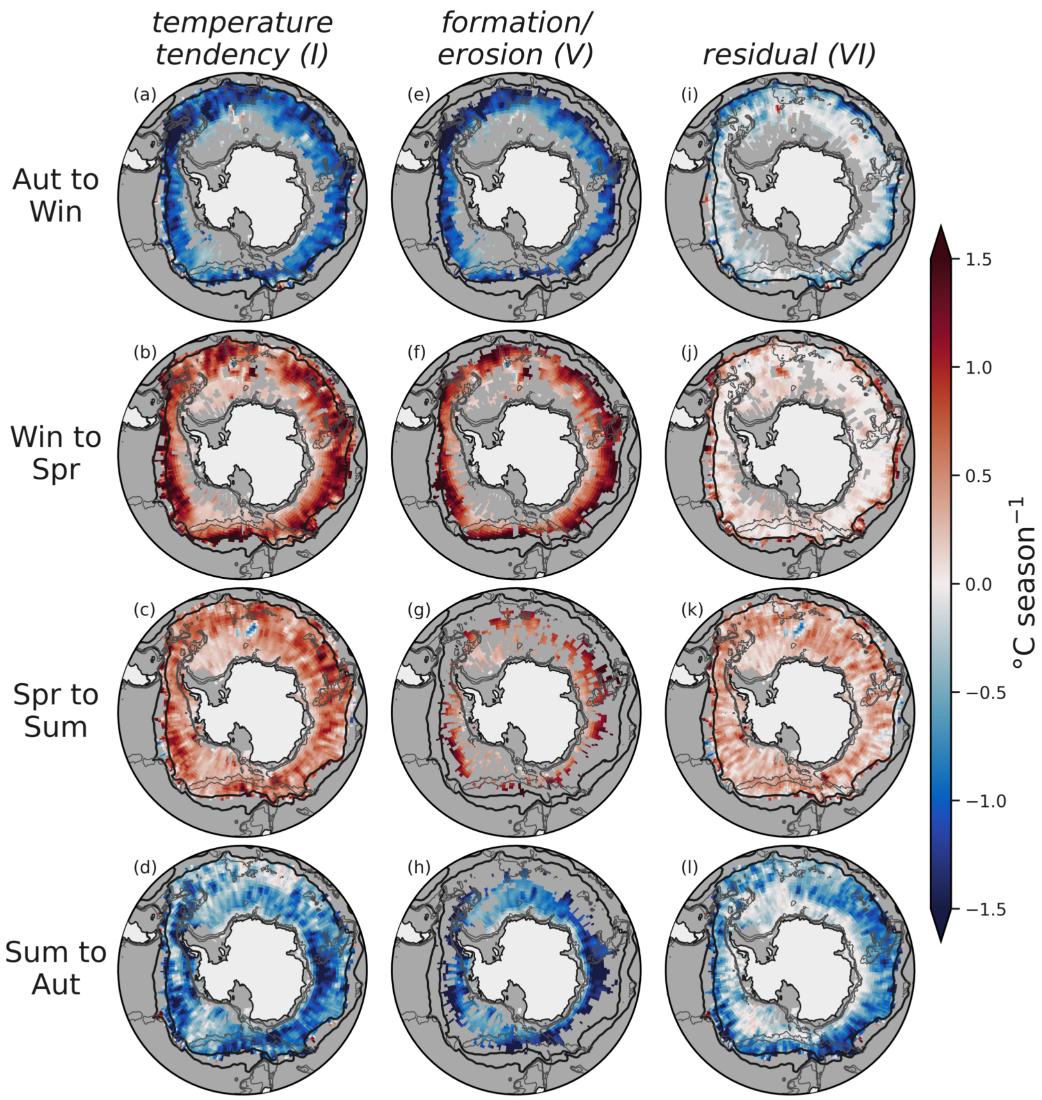


**Figure 8. Seasonal heat budget of subsurface Antarctic Winter Water.** (a-d) Temperature tendency where red (blue) indicates warming (cooling); (e-h) $WW_{SS}$ formation (blue) and erosion (red) terms; (i-l) residual where red (blue) indicates warming (cooling) via advection. The labels on the top of each row indicate the term from Equation 1. Black lines indicate the PF and SAF, and gray lines indicate 1km, 2km and 3km isobaths. All terms from Equation 1 are plotted in Figure S4 in Supporting Information.

sion takes place in the summer season, warming by 0.54 ± 0.74 °C season$^{-1}$ with smaller magnitude temperature tendency close to the Antarctic continent, such as in the Weddell Sea and Indian sector. Autumntime erosion of $WW_{SS}$ drives cooling of the $WW_{SS}$ system, especially close to the Antarctic continent in the regions where $WW_{ML}$ forms, for example southeast of KP (Figure 8h). Autumn has the largest removal of heat at -0.47 ± 1.12 °C season$^{-1}$ but only accounts for 37% of the temperature tendency.

The residual, which we assume is representative of advection and refer to it as such throughout this section, is of second order importance to the temperature tendency (Figures 8i-8l). In autumn and winter, $WW_{ML}$ and $WW_{SS}$ co-exist such that deep wintertime MLs, which experience a net heat loss, reside alongside $WW_{SS}$. Consequently, cold $WW_{ML}$ waters are advected into the $WW_{SS}$ and therefore cool the $WW_{SS}$. Conversely, in spring and summer the upper ocean is no longer cooling, and so $WW_{ML}$ is no longer forming. Therefore, advection drives warming of $WW_{SS}$ during spring and summer. In winter, surface cooling initiates the formation of $WW_{ML}$ and the subsequent equatorward advection, which results in a cooling of circumpolar $WW_{SS}$ by -0.33 ± 1.97 °C season$^{-1}$. This advection-driven cooling is largest close to the PF at the northern extent of WW where perennial $WW_{SS}$ exists throughout the entire annual cycle (Figures S1). Spring $WW_{SS}$ warms by 0.31 ± 0.92 °C season$^{-1}$, which largely takes place close to the PF. Summer has the largest magnitude mean warming via advection at 0.37 ± 0.69 °C season$^{-1}$ and is spatially homogeneous (Figure 8k). Advection in autumn drives the largest magnitude cooling with a seasonal mean of -0.47 ± 1.12 °C season$^{-1}$ (Figure 8l), but is low near the Antarctic continent due to erosion of $WW_{SS}$ (as shown by the formation term; Figure 8h). Spatial heterogeneity is observed in the autumntime residual term, with large magnitude signatures near KP, SEIR and downstream of PAR.

The additional terms (II, III, and IV) of Equation 1 are presented in Figure S4 in Supporting Information. Overall, these terms explain the remainder of the seasonal temperature tendency. Wind-driven mixing consistently warms $WW_{SS}$ across the circumpolar SO throughout the seasons in agreement with the findings of Giddy et al. (2023) (Figures S4e-S4h). Heightened wind-driven mixing is particularly evident across SEIR, where high winds are known to impart an enhanced wind-stress (Abernathey et al., 2011; Lin et al., 2018). The largest magnitude of $WW_{SS}$ warming due to wind-driven mixing occurs in autumn where there are the increased temperature gradients across the ML-WW boundary. Entrainment/detrainment varies based on the balance between warm CDW entrained into WW from below, driving warming, and heat removed from the WW layer through entrainment into the ML, thus cooling $WW_{SS}$. Substantial heterogeneous cooling of $WW_{SS}$ due to entrainment takes place in autumn in regions void of topographic features. This is coherent with deeper ML formation by ocean surface layer heat loss during autumn, particularly in the subantarctic ocean (Pellichero et al., 2017), driving entrainment of WW into the ML and the loss of heat from $WW_{SS}$.

The heat budget (Figure 8) provides key information to understand the seasonal change of $WW_{SS}$. We show that the cooling of $WW_{SS}$ takes place in autumn and winter whilst warming and mixing with the subsurface takes place in spring and summer, indicating the seasonal nature of heat fluxes in the upper SO and is potentially significant in water mass transformation (Abernathey et al., 2016; Evans et al., 2018; Pellichero et al., 2018).

### 3.2 Mechanisms Governing the Spatial Distribution of Antarctic Winter Water

Mean WW properties (Sections 3.1.2 and 3.1.3; Figures 4-7) exhibit broadscale characteristics that are relatively consistent throughout all properties across the SO: that is, quasi-homogeneous properties in the under-ice zone with meridional gradients in the open-ocean zone that, typically, increase in the northward direction. However, there exist re-

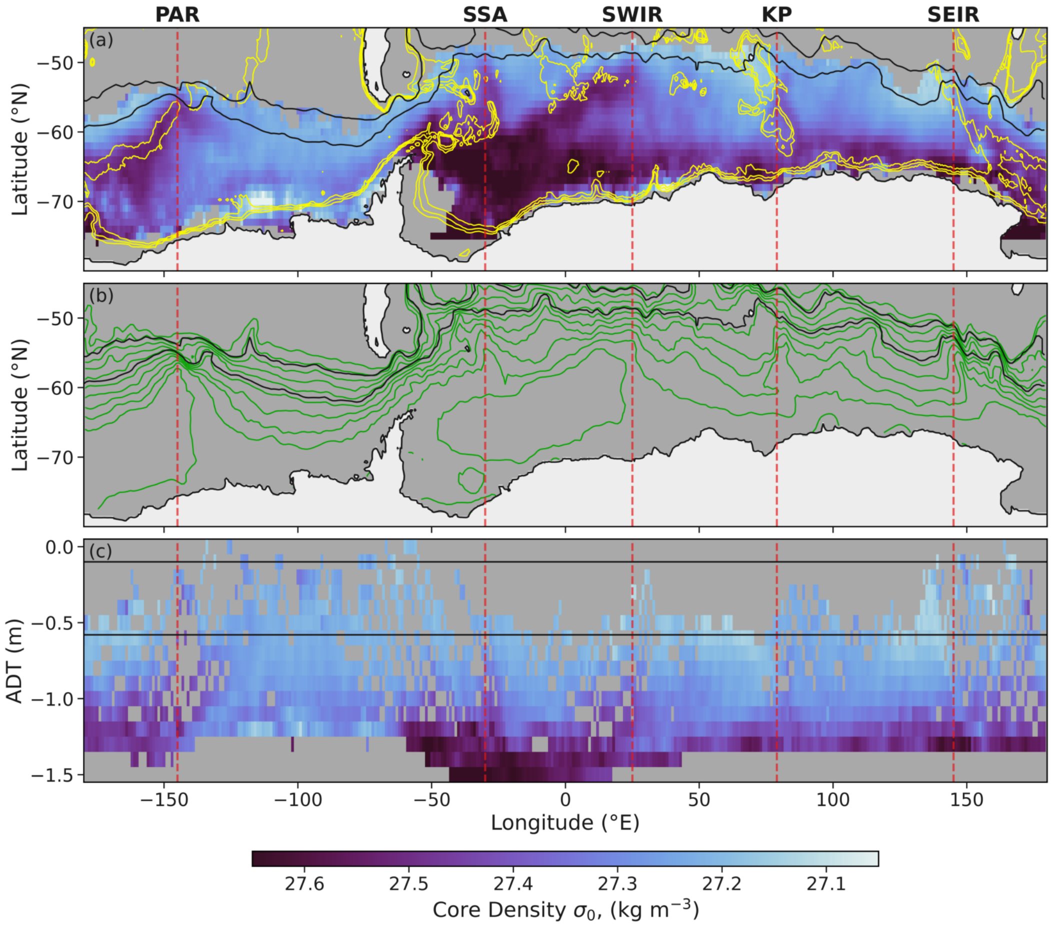


**Figure 9. Antarctic Winter Water core density.** (a) Annual mean WW core density. Yellow contours indicate 1km, 2km and 3km isobaths. (b) Absolute dynamic topography (ADT) streamlines are depicted in green. (c) Annual mean WW core density mapped onto ADT-Longitude coordinate space. (a-c) Black lines indicate the PF and SAF, and vertical dashed red lines show regions of topographic features, which are labeled as in Figure 2.

gions where properties associated with under-ice conditions appear to be transported northward, towards the PF. These regions of conserved under-ice properties in the open-ocean zone typically align with topographic features, and can be observed particularly clearly in the mean WW core density (Figure 9a) with dense WW cores in the open-ocean tightly constrained to the following topographic features: PAR, SSA, SWIR, KP, SEIR (west to east). In order to further investigate the spatial drivers of the large-scale properties of WW, we transform WW core density from latitude-longitude coordinate space to absolute dynamic topography (ADT)-longitude space (Figures 9c).

The distribution of WW is largely constrained to along-stream transport (referring to along-ADT streamlines). East of the PAR to the DP, in the open ocean ABS, WW is lighter in density (27.24 ± 0.10 kg m-3) and tightly constrained to ADT contours - a region where there is deep ocean bathymetry and few topographic features (the Pacific abyssal plane). Therefore, ocean interior mixing rates are lower than other parts of the SO (Frants et al., 2013; Ledwell et al., 2011), arresting densification of WW via reduced mixing with underlying CDW. Furthermore, CDW intrusions onto the ABS continental shelf results in a warm shelf basin (Narayanan et al., 2023; Tamsitt et al., 2021). Consequently, melt rates of sea ice are elevated in the region, as shown by the regionally fresh WW cores (see Section 3.2.2; Figures 4f and 7c). In the SO, salinity is the dominating contributor towards density (Roquet et al., 2022; Stewart & Haine, 2016). Thus, fresh WW cores lead to light WW core densities in the ABS.

Conversely, the Weddell Sea region is characterized by denser WW cores (27.43 ± 0.17 kg m-3, Figures 9) that advect northwards out of the Weddell Sea and across streamlines of SSH, following the southward edge of the SSA. Locations of across-stream transport align with topographic features throughout the SO, with the strongest across-stream signal observed at the SWIR (Figures 9c). The locations of elevated WW density extending equatorward reflect the pathways of northwards sea ice export (Haumann et al., 2016) and can potentially play a critical role in redistributing CDW and sea ice-driven brine properties. Further, WW core density reflects the northward advection of surface waters from the Weddell Sea where the SSA is a region known for high rates of surface advection, as is reflected by iceberg pathways (Budge & Long, 2018), and understood in observational studies via the use of the geostrophic thermal wind relation (Katsumata & Yoshinari, 2010; Oke et al., 2022).

Dense WW extending northward is observed close to the SWIR, which is likely a result of the Weddell Gyre northward circulation advecting WW northwards. Similarly, dense WW is transported northwards across the PAR, which is facilitated by the Ross Gyre; Zilberman et al. (2017) show similar findings of equatorward transport of ocean interior water masses such as Subantarctic Mode Water north of the ACC. Moreover, the regions of across-stream transport of WW coincide with the bathymetrically steered export pathways of Antarctic Bottom Water, as detailed by Solodoch et al. (2022) as well as others (Kusahara et al., 2017; Meredith, 2013; van Sebille et al., 2013). This also agrees with property transport preferentially facilitated by transient eddies, which are more probable to be present in regions of large bathymetric features and high EKE (Naveira Garabato et al., 2011; Thompson & Sallée, 2012; Wilson et al., 2022).

# 4 Assumptions and Limitations

## 4.1 Data Limitations

Hydrographic data in the Southern Ocean is prone to patchy spatiotemporal distributions (Figures 2a-2d and 2i). Certain regions have low data coverage, such as the Pacific sector and within the seasonal ice zone. Many factors impact the distribution of data, for example, ship transects determine ship-based CTD cast time and location as well as float deployments. Also, floats being largely Lagrangian are steered and entrained by the dominant ACC fronts (Figures 2e-2h), which leads to a somewhat reduced sampling of inter-frontal zones subject to reduced current strengths or shallower areas due to topographic steering (Kamenkovich et al., 2017). Nonetheless, profiling floats provide impressively broad coverage of the circumpolar SO (Figure 2j). Furthermore, MEOP is an important dataset that provides near full annual coverage in the southern domains of the SO and sea ice regions (Figures 2a-2h). However, seal behavior restricts broad and unbiased geographically coverage, resulting in observation hotspots (for example, the Western Antarctic Peninsula in ABS and KP). Further biases are introduced due to foraging preferences since seals favor frontal peripheries and regions that experience less intense surface warming (Siegelman et al., 2019; Azarian et al., 2024). The data included coincide with the Weddell Sea polynya years of 2016 and 2017 (Figures 2g and 2i), which results in a localized sampling bias of the warm water column over Maud Rise (∼65°S, 3°E) (Gülk et al., 2023; Mohrmann et al., 2022).

The ocean is also temporally variable, as noted by the differences in WW characteristics shown in the varying seasons. Certain regions, particularly the sea ice impacted ocean, have locations of limited profiles (e.g. less than 20) in the seasonal climatology of 18 years. An implication of this is that should any interannual variability exist in the WW characteristics, there is likely to be a bias towards the characteristics of the particular period sampled. Furthermore, should there be a bias in a given month sampled, e.g., more profiles existed in February during the summer climatology for a given region, then there would likely be a bias towards thinner, warmer $\mathrm{WW_{SS}}$, as indicated by the seasonal evolution shown in this study. Such aspects around spatiotemporal data coverage means that the characteristics of WW are not always consistently described in space and time, particularly in the permanent sea ice regions of the Weddell and Ross Seas and on parts of continental shelves. Nonetheless, to date, data coverage is at a status which allows robust descriptions and heat budget calculations over the vast majority of circumpolar SO and at a seasonal temporal resolution. The expected increase in observations and spatial coverage, particularly due to the onset or growth of various programmes, such as SOCCOM and MEOP (Figures 2i and 2j) will further narrow these observational gaps in the coming years to better resolve aspects around interannual variability or finer scale processes modulating WW.

### 4.2 Heat Budget Methodology

The heat budget work we have conducted provides information, for the first time, of the role $\mathrm{WW_{SS}}$ plays in redistributing heat in the upper SO and how this varies seasonally (Section 3.3). Below, we cover the assumptions made in the heat budget computation and methodology (Section 2.3). When calculating the down-ward turbulent heat flux (Term (III), Equation 1), we use the correlation found by Nicholson et al. (2022) between theoretical dissipation and observed summertime dissipation. Thus, we make the assumption that this correlation holds for the circumpolar SO across the annual cycle. The seasonal period is important because buoyancy plays a minor role in internal mixing in the summer period due to stratifying the water column whereas buoyancy destratifies the ML and drives convection in winter, resulting in both convection and shear driving the dissipation of turbulent kinetic energy (Sohail et al., 2018). Since we only apply our diffusivity parameterization to the open-ocean zone (north of the 15% sea ice concentration) and to $\mathrm{WW_{SS}}$, the wintertime mixing terms contributes a small portion of the heat budget (<10% for winter; Figure S4). Nonetheless, we find our diffusivity results to be comparable across the SO, which is of the $\mathrm{O}(10^{-5})$ (Wu et al., 2011). Furthermore, localized results agree with observations up- and downstream of DP, where mixing regimes differ due to topographically enhanced mixing (Frants et al., 2013; Merrifield et al., 2016; Whalen et al., 2012). We further cross-referenced our heat budget findings with that of Giddy et al. (2023), whose mean January heat flux of 15 W m$^{-2}$ in (60 °S, 0 °E) from observations agrees with our estimates. Thus, whilst this methodology is based on assumptions with propagating uncertainties, it is a development from existing methodologies (Pellichero et al., 2017), who use a constant diffusivity term, whereas we have used a spatiotemporally varying term that, to a first approximation, takes into account spatiotemporal variation in wind forcing and ocean stratification.

## 5 Conclusion

This study investigates Antarctic Winter Water (WW) across the circumpolar SO using over 600,000 in-situ hydrographic observations across 18 years (Figure 2). We evaluate the various physical mechanisms that impact the spatiotemporal distribution of WW, as conceptually portrayed in Figure 1. We have shown that the annual cycle of WW varies seasonally with sea ice growth such that $WW_{ML}$ forms below sea ice during sea ice formation periods and is capped following ML restratification to form $WW_{SS}$ as sea ice melts (Figure 3). Furthermore, we found that the properties of WW (core temperature, core salinity, core depth, and thickness) vary seasonally with distinct annual cycles (Figures 4 and 6). However, annual means exhibit similar spatial distributions such that WW properties are largely homogenous below sea ice (south of the 15% sea ice concentration extent; Figures 4-6), with meridional gradients when north of sea ice. We find that WW properties associated with under-ice characteristics are transported equatorwards near large topographic features, such as the Pacific Antarctic Ridge, South Sandwich Trench, Southwest Indian Ridge, Kerguelen Plateau and Southeast Indian Ridge. We find that these regions show dense WW that flow across SSH streamlines (Figures 9), which is indicative of elevated velocities in the equatorward direction (through the thermal wind relation), transporting subpolar properties at different rates seasonally (Figure 8). Hence, equatorward redistribution of under-ice associated WW properties is largely driven by topographic steering, agreeing with findings of bathymetrically steered export pathways of Antarctic Bottom Water (Solodoch et al., 2022) to the global ocean.

This work provides a basis for future WW studies and raises many questions regarding the role WW plays in the upper ocean and overturning circulation. For example, whether subpolar properties are transported to the global ocean through the energetic ACC via eddies and whether the properties are retained or mixed away. Further studies on CDW-WW interactions will help to gain an understanding of how ocean interior properties interact with the surface ocean. Critically, this work identifies potential meridional pathways for the upper limb of the overturning circulation and provides additional evidence to support heterogeneous and seasonal localized overturning pathways, developing from the zonal mean overturning framework.

## Open Research

All computer code and the quality controlled, vertically gridded hydrographic profiles are available in open-access repositories (Spira et al., 2023; Spira, 2024). The various hydrographic data were collated from the following programmes: the International Argo Program provided the Argo floats hydrographic data (`https://portal.aodn.org.au`); the marine mammal hydrographic data were sourced from the International MEOP Consortium and the national programs that contribute to it (`http://meop.net`); the Southern Ocean biogeochemical float hydrographic data were provided by SOCCOM (`https://soccom.princeton.edu/`); the hydrographic ship-based CTD casts and glider profiles were provided by NOAA WOD (`https://www.nodc.noaa.gov/OC5/SELECT/dbsearch/dbsearch.html`). ERA5 data are generated using Copernicus Climate Change Service Information, available online at www.ecmwf.int/en/forecasts/datasets/archive-datasets/reanalysis-datasets/era5. The sea-ice data are made available via `http://data.meereisportal.de/data/iup/hdf/s/`. The ADT data used to determine the fronts are generated by the Archiving, Validation, and Interpretation of Satellite Oceanographic data service of Centre National D'Etudes Spatiales, available online `www.aviso.altimetry.fr/en/data/data-access/`

`gridded-data-extraction-tool.html`. Bathymetry data is available by GEBCO Compilation Group (GEBCO, 2023).

## Acknowledgments

We would like to acknowledge the significant efforts made to collect the various public access hydrographic observations made available by programmes such as Argo, MEOP, SOCCOM, WOD18, and glider and ship-based campaigns, that we utilize in this study. T.S and S.S are supported by a Wallenberg Academy Fellowship (WAF 2015.0186) and the Swedish Research Council (VR 2019-04400) grant of S.S. S.S. and M.D.d.P. have received funding from the European Union's Horizon 2020 research and innovation program under grant agreement no. 821001 (SO-CHIC). M.D.d.P. is supported by the European Union's Marie Sklodowska Curie Individual Fellowship under Project ID 101032683. I.G. is supported by the Post Doctoral Fellowship grant of the Swedish Research Council (2022-00395).

## References

Abernathey, R., Cerovecki, I., Holland, P. R., Newsom, E., Mazloff, M., & Talley, L. D. (2016). Water-mass transformation by sea ice in the upper branch of the southern ocean overturning. *Nature Geoscience*, *9*(8), 596–601. doi: 10.1038/ngeo2749

Abernathey, R., Marshall, J., & Ferreira, D. (2011). The Dependence of Southern Ocean Meridional Overturning on Wind Stress. *Journal of Physical Oceanography*, *41*(12), 2261–2278. doi: 10.1175/JPO-D-11-023.1

Azarian, C., Bopp, L., Sallée, J.-B., Swart, S., Guinet, C., & d'Ovidio, F. (2024). Marine heatwaves and global warming impacts on winter waters in the Southern Indian Ocean. *Journal of Marine Systems*, *243*, 103962. doi: 10.1016/j.jmarsys.2023.103962

Bebieva, Y., & Speer, K. (2019). The Regulation of Sea Ice Thickness by Double-Diffusive Processes in the Ross Gyre. *Journal of Geophysical Research: Oceans*, *124*(10), 7068–7081. doi: 10.1029/2019JC015247

Belkin, I. M., & Gordon, A. L. (1996). Southern Ocean fronts from the Greenwich meridian to Tasmania. *Journal of Geophysical Research: Oceans*, *101*(C2), 3675–3696. doi: 10.1029/95JC02750

Biddle, L. C., & Swart, S. (2020). The Observed Seasonal Cycle of Submesoscale Processes in the Antarctic Marginal Ice Zone. *Journal of Geophysical Research: Oceans*, *125*(6). doi: 10.1029/2019JC015587

Boland, E. J. D., Jones, D. C., Meijers, A. J. S., Forget, G., & Josey, S. A. (2021). Local and Remote Influences on the Heat Content of Southern Ocean Mode Water Formation Regions. *Journal of Geophysical Research: Oceans*, *126*(4), e2020JC016585. doi: 10.1029/2020JC016585

Bouffard, D., & Boegman, L. (2013). A diapycnal diffusivity model for stratified environmental flows. *Dynamics of Atmospheres and Oceans*, *61-62*, 14–34. doi: 10.1016/j.dynatmoce.2013.02.002

Boyer, T., Baranova, C., Coleman, H. E., Garcia, A., Grodsky, R. A., Locarnini, A. V., ... Zweng (2018). *World Ocean Database 2018.* [Dataset].

Boyer, T., Zhang, H.-M., O'Brien, K., Reagan, J., Diggs, S., Freeman, E., ... others (2023). Effects of the pandemic on observing the global ocean. *Bulletin of the American Meteorological Society*, *104*(2), E389–E410.

Brett, A., Leape, J., Abbott, M., Sakaguchi, H., Cao, L., Chand, K., ... Myksvoll, M. S. (2020). Ocean data need a sea change to help navigate the warming world. *Nature*, *582*(7811), 181–183. doi: 10.1038/d41586-020-01668-z

Budge, J. S., & Long, D. G. (2018). A Comprehensive Database for Antarctic Iceberg Tracking Using Scatterometer Data. *IEEE Journal of Selected Topics in*

*Applied Earth Observations and Remote Sensing*, *11*(2), 434–442. doi: 10.1109/JSTARS.2017.2784186

Caneill, R., Roquet, F., & Nycander, J. (2023). Southern Ocean deep mixing band emerges from a competition between winter buoyancy loss and upper stratification strength. *EGUsphere*, *2023*, 1–29. doi: 10.5194/egusphere-2023-2404

Cerovečki, I., Talley, L. D., Mazloff, M. R., & Maze, G. (2013). Subantarctic Mode Water Formation, Destruction, and Export in the Eddy-Permitting Southern Ocean State Estimate. *Journal of Physical Oceanography*, *43*(7), 1485–1511. doi: 10.1175/JPO-D-12-0121.1

de Boyer Montégut, C. (2004). Mixed layer depth over the global ocean: An examination of profile data and a profile-based climatology. *Journal of Geophysical Research*, *109*(C12), C12003. doi: 10.1029/2004JC002378

Dong, S., Sprintall, J., Gille, S. T., & Talley, L. (2008). Southern Ocean mixed-layer depth from Argo float profiles. *Journal of Geophysical Research*, *113*(C6), C06013. doi: 10.1029/2006JC004051

Dotto, T. S., Heywood, K. J., Hall, R. A., Scambos, T. A., Zheng, Y., Nakayama, Y., ... Pettit, E. (2022). Ocean variability beneath Thwaites Eastern Ice Shelf driven by the Pine Island Bay Gyre strength. *Nature Communications*, *13*(1), 7840. doi: 10.1038/s41467-022-35499-5

Dotto, T. S., Naveira Garabato, A., Bacon, S., Tsamados, M., Holland, P. R., Hooley, J., ... Meredith, M. P. (2018). Variability of the Ross Gyre, Southern Ocean: Drivers and Responses Revealed by Satellite Altimetry. *Geophysical Research Letters*, *45*(12), 6195–6204. doi: 10.1029/2018GL078607

Dove, L. A., Balwada, D., Thompson, A. F., & Gray, A. R. (2022). Enhanced Ventilation in Energetic Regions of the Antarctic Circumpolar Current. *Geophysical Research Letters*, *49*(13), e2021GL097574. doi: 10.1029/2021GL097574

Drake, H. F., Morrison, A. K., Griffies, S. M., Sarmiento, J. L., Weijer, W., & Gray, A. R. (2018). Lagrangian Timescales of Southern Ocean Upwelling in a Hierarchy of Model Resolutions. *Geophysical Research Letters*, *45*(2), 891–898. doi: 10.1002/2017GL076045

du Plessis, M., Swart, S., Ansorge, I. J., & Mahadevan, A. (2017). Submesoscale processes promote seasonal restratification in the subantarctic ocean. *Journal of Geophysical Research: Oceans*, *122*(4), 2960–2975. doi: 10.1002/2016JC012494

du Plessis, M., Swart, S., Biddle, L. C., Giddy, I. S., Monteiro, P. M. S., Reason, C. J. C., ... Nicholson, S. (2022). The Daily-Resolved Southern Ocean Mixed Layer: Regional Contrasts Assessed Using Glider Observations. *Journal of Geophysical Research: Oceans*, *127*(4). doi: 10.1029/2021JC017760

Evans, D. G., Zika, J. D., Naveira Garabato, A. C., & Nurser, A. J. G. (2018). The Cold Transit of Southern Ocean Upwelling. *Geophysical Research Letters*, *45*(24). doi: 10.1029/2018GL079986

Frants, M., Damerell, G. M., Gille, S. T., Heywood, K. J., MacKinnon, J., & Sprintall, J. (2013). An Assessment of Density-Based Finescale Methods for Estimating Diapycnal Diffusivity in the Southern Ocean. *Journal of Atmospheric and Oceanic Technology*, *30*(11), 2647–2661. doi: 10.1175/JTECH-D-12-00241.1

Ganachaud, A., & Wunsch, C. (2000). Improved estimates of global ocean circulation, heat transport and mixing from hydrographic data. *Nature*, *408*(6811), 453–457. doi: 10.1038/35044048

GEBCO. (2023). GEBCO 2023 grid [Dataset]. *(GEBCO Compilation Group)*. doi: 10.5285/f98b053b-6100cbc-6c23-e053-6c86abc0af7b

Giddy, I. S., Fer, I., Swart, S., & Nicholson, S.-A. (2023). Vertical Convergence of Turbulent and Double-Diffusive Heat Flux Drives Warming and Erosion of Antarctic Winter Water in Summer. *Journal of Physical Oceanography*, *53*(8), 1941–1958. doi: 10.1175/JPO-D-22-0259.1

Goosse, H., Allende Contador, S., Bitz, C. M., Blanchard-Wrigglesworth, E., Eayrs, C., Fichefet, T., ... van Lipzig, N. P. M. (2023). Modulation of the seasonal cycle of the Antarctic sea ice extent by sea ice processes and feedbacks with the ocean and the atmosphere. *The Cryosphere*, *17*(1), 407–425. doi: 10.5194/tc-17-407-2023

Gordon, A. L., & Huber, B. A. (1984). Thermohaline stratification below the southern ocean sea ice. *Journal of Geophysical Research: Oceans*, *89*(C1), 641–648.

Gregg, M., D'Asaro, E., Riley, J., & Kunze, E. (2018). Mixing Efficiency in the Ocean. *Annual Review of Marine Science*, *10*(1), 443–473. doi: 10.1146/annurev-marine-121916-063643

Groeskamp, S., Abernathey, R. P., & Klocker, A. (2016). Water mass transformation by cabbeling and thermobaricity. *Geophysical Research Letters*, *43*(20), 10,835–10,845. doi: 10.1002/2016GL070860

Gülk, B., Roquet, F., Naveira Garabato, A. C., Narayanan, A., Rousset, C., & Madec, G. (2023). Variability and Remote Controls of the Warm-Water Halo and Taylor Cap at Maud Rise. *Journal of Geophysical Research: Oceans*, *128*(7), e2022JC019517. doi: 10.1029/2022JC019517

Haumann, F. A., Gruber, N., Münnich, M., Frenger, I., & Kern, S. (2016). Sea-ice transport driving Southern Ocean salinity and its recent trends. *Nature*, *537*(7618), 89–92. doi: 10.1038/nature19101

Herraiz-Borreguero, L., & Rintoul, S. R. (2011). Subantarctic mode water: distribution and circulation. *Ocean Dynamics*, *61*(1), 103–126. doi: 10.1007/s10236-010-0352-9

Hersbach, H., Bell, B., Berrisford, P., Biavati, G., Horányi, A., Muñoz Sabater, J., ... Thépaut, J.-N. (2023). Era5 monthly averaged data on single levels from 1940 to present. *Copernicus Climate Change Service (C3S) Climate Data Store (CDS).* (Accessed on 01-06-2023) doi: 10.24381/cds.f17050d7

Hirano, D., Kitade, Y., Nagashima, H., & Matsuyama, M. (2010). Characteristics of observed turbulent mixing across the Antarctic Slope Front at 140°E, East Antarctica. *Journal of Oceanography*, *66*(1), 95–104. doi: 10.1007/s10872-010-0008-x

Holland, P. R. (2014). The seasonality of Antarctic sea ice trends. *Geophysical Research Letters*, *41*(12), 4230–4237. doi: 10.1002/2014GL060172

Holland, P. R., Bruneau, N., Enright, C., Losch, M., Kurtz, N. T., & Kwok, R. (2014). Modeled Trends in Antarctic Sea Ice Thickness. *Journal of Climate*, *27*(10), 3784–3801. doi: 10.1175/JCLI-D-13-00301.1

Huguenin, M. F., Holmes, R. M., & England, M. H. (2022). Drivers and distribution of global ocean heat uptake over the last half century. *Nature Communications*, *13*(1), 4921. doi: 10.1038/s41467-022-32540-5

Jacobs, S. S. (2004). Bottom water production and its links with the thermohaline circulation. *Antarctic Science*, *16*(4), 427–437. doi: 10.1017/S095410200400224X

Johnson, G. C. (2008). Quantifying Antarctic Bottom Water and North Atlantic Deep Water volumes. *Journal of Geophysical Research: Oceans*, *113*(C5). doi: 10.1029/2007JC004477

Jones, D. C., Sonnewald, M., Zhou, S., Hausmann, U., Meijers, A. J. S., Rosso, I., ... Naveira Garabato, A. C. (2023). Unsupervised classification identifies coherent thermohaline structures in the Weddell Gyre region. *Ocean Science*, *19*(3), 857–885. doi: 10.5194/os-19-857-2023

Kamenkovich, I., Haza, A., Gray, A. R., Dufour, C. O., & Garraffo, Z. (2017). Observing System Simulation Experiments for an array of autonomous biogeochemical profiling floats in the Southern Ocean. *Journal of Geophysical Research: Oceans*, *122*(9), 7595–7611. doi: 10.1002/2017JC012819

Karstensen, J. (2004). Formation of the South Pacific Shallow Salinity Minimum: A Southern Ocean Pathway to the Tropical Pacific. *Journal of Physical Oceanography*, *34*(11), 2398–2412. doi: 10.1175/JPO2634.1

Katsumata, K., & Yoshinari, H. (2010). Uncertainties in global mapping of Argo drift data at the parking level. *Journal of Oceanography*, *66*(4), 553–569. doi: 10.1007/s10872-010-0046-4

Kusahara, K., Williams, G. D., Tamura, T., Massom, R., & Hasumi, H. (2017). Dense shelf water spreading from Antarctic coastal polynyas to the deep Southern Ocean: A regional circumpolar model study. *Journal of Geophysical Research: Oceans*, *122*(8), 6238–6253. doi: 10.1002/2017JC012911

Ledwell, J. R., Laurent, L. C. S., Girton, J. B., & Toole, J. M. (2011). Diapycnal Mixing in the Antarctic Circumpolar Current. *Journal of Physical Oceanography*, *41*(1), 241–246. doi: 10.1175/2010JPO4557.1

Li, Z., England, M. H., Groeskamp, S., Cerovečki, I., & Luo, Y. (2021). The Origin and Fate of Subantarctic Mode Water in the Southern Ocean. *Journal of Physical Oceanography*. doi: 10.1175/JPO-D-20-0174.1

Lin, X., Zhai, X., Wang, Z., & Munday, D. R. (2018). Mean, Variability, and Trend of Southern Ocean Wind Stress: Role of Wind Fluctuations. *Journal of Climate*, *31*(9), 3557–3573. doi: 10.1175/JCLI-D-17-0481.1

Lund, D. C., Chase, Z., Kohfeld, K. E., & Wilson, E. A. (2021). Tracking Southern Ocean Sea Ice Extent With Winter Water: A New Method Based on the Oxygen Isotopic Signature of Foraminifera. *Paleoceanography and Paleoclimatology*, *36*(6), e2020PA004095. doi: 10.1029/2020PA004095

Mahadevan, A., & Campbell, J. W. (2002). Biogeochemical patchiness at the sea surface: BIOGEOCHEMICAL PATCHINESS AT SEA SURFACE. *Geophysical Research Letters*, *29*(19), 32–1–32–4. doi: 10.1029/2001GL014116

Marshall, J., & Speer, K. (2012). Closure of the meridional overturning circulation through Southern Ocean upwelling. *Nature Geoscience*, *5*(3), 171–180. doi: 10.1038/ngeo1391

Martinson, D. G. (1990). Evolution of the southern ocean winter mixed layer and sea ice: Open ocean deepwater formation and ventilation. *Journal of Geophysical Research: Oceans*, *95*(C7), 11641–11654. doi: 10.1029/JC095iC07p11641

Mashayek, A., Ferrari, R., Merrifield, S., Ledwell, J. R., St Laurent, L., & Garabato, A. N. (2017). Topographic enhancement of vertical turbulent mixing in the Southern Ocean. *Nature Communications*, *8*(1), 14197. doi: 10.1038/ncomms14197

McMahon, C. R., Hindell, M. A., Charrassin, J.-B., Corney, S., Guinet, C., Harcourt, R., … Bestley, S. (2019). Finding mesopelagic prey in a changing Southern Ocean. *Scientific Reports*, *9*(1), 19013. doi: 10.1038/s41598-019-55152-4

McWilliams, J. C. (2021). Oceanic Frontogenesis. *Annual Review of Marine Science*, *13*(1), 227–253. doi: 10.1146/annurev-marine-032320-120725

Meijers, A. J. S., Cerovečki, I., King, B. A., & Tamsitt, V. (2019). A See-Saw in Pacific Subantarctic Mode Water Formation Driven by Atmospheric Modes. *Geophysical Research Letters*, *46*(22), 13152–13160. doi: 10.1029/2019GL085280

Meredith, M. P. (2013). Replenishing the abyss. *Nature Geoscience*, *6*(3), 166–167. doi: 10.1038/ngeo1743

Merrifield, S. T., Laurent, L. S., Owens, B., Thurnherr, A. M., & Toole, J. M. (2016). Enhanced Diapycnal Diffusivity in Intrusive Regions of the Drake Passage. *Journal of Physical Oceanography*, *46*(4), 1309–1321. doi: 10.1175/JPO-D-15-0068.1

Mohrmann, M., Heuzé, C., & Swart, S. (2021). Southern Ocean polynyas in CMIP6 models. *The Cryosphere*, *15*(9), 4281–4313. doi: 10.5194/tc-15-4281-2021

Mohrmann, M., Swart, S., & Heuzé, C. (2022). Observed mixing at the flanks of Maud Rise in the Weddell Sea. *Geophysical Research Letters*, *49*(8), e2022GL098036. doi: 10.1029/2022GL098036

Morales Maqueda, M. A., Willmott, A. J., & Biggs, N. R. T. (2004). Polynya

Dynamics: a Review of Observations and Modeling. *Reviews of Geophysics*, *42*(1). doi: 10.1029/2002RG000116

Morrison, A. K., Griffies, S. M., Winton, M., Anderson, W. G., & Sarmiento, J. L. (2016). Mechanisms of Southern Ocean Heat Uptake and Transport in a Global Eddying Climate Model. *Journal of Climate*, *29*(6), 2059–2075. doi: 10.1175/JCLI-D-15-0579.1

Morrow, R., Valladeau, G., & Sallee, J.-B. (2008). Observed subsurface signature of Southern Ocean sea level rise. *Progress in Oceanography*, *77*(4), 351–366. doi: 10.1016/j.pocean.2007.03.002

Munk, W. H. (1966). Abyssal recipes. In *Deep sea research and oceanographic abstracts* (Vol. 13, pp. 707–730).

Nakayama, Y., Menemenlis, D., Zhang, H., Schodlok, M., & Rignot, E. (2018). Origin of Circumpolar Deep Water intruding onto the Amundsen and Bellingshausen Sea continental shelves. *Nature Communications*, *9*(1), 3403. doi: 10.1038/s41467-018-05813-1

Narayanan, A., Gille, S. T., Mazloff, M. R., du Plessis, M. D., Murali, K., & Roquet, F. (2023). Zonal Distribution of Circumpolar Deep Water Transformation Rates and Its Relation to Heat Content on Antarctic Shelves. *Journal of Geophysical Research: Oceans*, *128*(6), e2022JC019310. doi: 10.1029/2022JC019310

Naveira Garabato, A. C., Ferrari, R., & Polzin, K. L. (2011). Eddy stirring in the Southern Ocean. *Journal of Geophysical Research: Oceans*, *116*(C9). doi: 10.1029/2010JC006818

Nicholson, S.-A., Whitt, D. B., Fer, I., Du Plessis, M. D., Lebéhot, A. D., Swart, S., … Monteiro, P. M. S. (2022). Storms drive outgassing of CO2 in the subpolar Southern Ocean. *Nature Communications*, *13*(1), 158. doi: 10.1038/s41467-021-27780-w

Nikurashin, M., Vallis, G. K., & Adcroft, A. (2013). Routes to energy dissipation for geostrophic flows in the Southern Ocean. *Nature Geoscience*, *6*(1), 48–51. doi: 10.1038/ngeo1657

Oke, P. R., Rykova, T., Pilo, G. S., & Lovell, J. L. (2022). Estimating Argo Float Trajectories Under Ice. *Earth and Space Science*, *9*(7), e2022EA002312. doi: 10.1029/2022EA002312

Orsi, A. H., Whitworth, T., & Nowlin, W. D. (1995). On the meridional extent and fronts of the Antarctic Circumpolar Current. *Deep Sea Research Part I: Oceanographic Research Papers*, *42*(5), 641–673. doi: 10.1016/0967-0637(95)00021-W

Osborn, T. R. (1980). Estimates of the Local Rate of Vertical Diffusion from Dissipation Measurements. *Journal of Physical Oceanography*, *10*(1), 83–89. doi: 10.1175/1520-0485(1980)010⟨0083:EOTLRO⟩2.0.CO;2

Park, Y.-H., Charriaud, E., & Fieux, M. (1998). Thermohaline structure of the Antarctic Surface Water/Winter Water in the Indian sector of the Southern Ocean. *Journal of Marine Systems*, *17*(1-4), 5–23.

Park, Y.-H., Charriaud, E., Pino, D. R., & Jeandel, C. (1998). Seasonal and interannual variability of the mixed layer properties and steric height at station KERFIX, southwest of Kerguelen. *Journal of Marine Systems*, *17*(1-4), 571–586.

Park, Y.-H., Park, T., Kim, T.-W., Lee, S.-H., Hong, C.-S., Lee, J.-H., … Provost, C. (2019). Observations of the Antarctic Circumpolar Current Over the Udintsev Fracture Zone, the Narrowest Choke Point in the Southern Ocean. *Journal of Geophysical Research: Oceans*, *124*(7), 4511–4528. doi: 10.1029/2019JC015024

Park, Y.-H., Vivier, F., Roquet, F., & Kestenare, E. (2009). Direct observations of the ACC transport across the Kerguelen Plateau. *Geophysical Research Letters*, *36*(18). doi: 10.1029/2009GL039617

Paulson, C. A., & Simpson, J. J. (1977). Irradiance Measurements in the Upper Ocean. *Journal of Physical Oceanography*, *7*(6), 952–956. doi: 10.1175/1520-0485(1977)007⟨0952:IMITUO⟩2.0.CO;2

Pellichero, V., Sallée, J.-B., Chapman, C. C., & Downes, S. M. (2018). The southern ocean meridional overturning in the sea-ice sector is driven by freshwater fluxes. *Nature Communications*, *9*(1), 1789. doi: 10.1038/s41467-018-04101-2

Pellichero, V., Sallée, J.-B., Schmidtko, S., Roquet, F., & Charrassin, J.-B. (2017). The ocean mixed layer under Southern Ocean sea-ice: Seasonal cycle and forcing: OCEAN MIXED LAYER UNDER SOUTHERN SEA-ICE. *Journal of Geophysical Research: Oceans*, *122*(2), 1608–1633. doi: 10.1002/2016JC011970

Pollard, R. T., Lucas, M. I., & Read, J. F. (2002). Physical controls on biogeochemical zonation in the Southern Ocean. *Deep Sea Research Part II: Topical Studies in Oceanography*, *49*(16), 3289–3305. doi: 10.1016/S0967-0645(02)00084-X

Roquet, F., Ferreira, D., Caneill, R., Schlesinger, D., & Madec, G. (2022). Unique thermal expansion properties of water key to the formation of sea ice on Earth. *Science Advances*, *8*(46), eabq0793. doi: 10.1126/sciadv.abq0793

Rosso, I., Hogg, A. M., Kiss, A. E., & Gayen, B. (2015). Topographic influence on submesoscale dynamics in the Southern Ocean. *Geophysical Research Letters*, *42*(4), 1139–1147. doi: 10.1002/2014GL062720

Rosso, I., Hogg, A. M., Strutton, P. G., Kiss, A. E., Matear, R., Klocker, A., & Van Sebille, E. (2014). Vertical transport in the ocean due to sub-mesoscale structures: Impacts in the Kerguelen region. *Ocean Modelling*, *80*, 10–23. doi: 10.1016/j.ocemod.2014.05.001

Sabu, P., Libera, S. A., Chacko, R., Anilkumar, N., Subeesh, M., & Thomas, A. P. (2020). Winter water variability in the Indian Ocean sector of Southern Ocean during austral summer. *Deep Sea Research Part II: Topical Studies in Oceanography*, *178*, 104852. doi: 10.1016/j.dsr2.2020.104852

Sarmiento, J. L., Johnson, K. S., Arteaga, L. A., Bushinsky, S. M., Cullen, H. M., Gray, A. R., … Talley, L. D. (2023). The Southern Ocean carbon and climate observations and modeling (SOCCOM) project: A review. *Progress in Oceanography*, *219*, 103130. doi: 10.1016/j.pocean.2023.103130

Shaw, W. J., & Stanton, T. P. (2014). Dynamic and Double-Diffusive Instabilities in a Weak Pycnocline. Part I: Observations of Heat Flux and Diffusivity in the Vicinity of Maud Rise, Weddell Sea. *Journal of Physical Oceanography*, *44*(8), 1973–1991. doi: 10.1175/JPO-D-13-042.1

Siegelman, L., O'Toole, M., Flexas, M., Rivière, P., & Klein, P. (2019). Submesoscale ocean fronts act as biological hotspot for southern elephant seal. *Scientific Reports*, *9*(1), 5588. doi: 10.1038/s41598-019-42117-w

SOCCOM. (2019). Southern ocean carbon and climate observations and modelling. [Dataset]. *(SOCCOM)*. (Retrieved from `https://soccom.princeton.edu/`)

Sohail, T., Gayen, B., & Hogg, A. M. (2018). Convection Enhances Mixing in the Southern Ocean. *Geophysical Research Letters*, *45*(9), 4198–4207. doi: 10.1029/2018GL077711

Solodoch, A., Stewart, A. L., Hogg, A. M., Morrison, A. K., Kiss, A. E., Thompson, A. F., … Cimoli, L. (2022). How Does Antarctic Bottom Water Cross the Southern Ocean? *Geophysical Research Letters*, *49*(7), e2021GL097211. doi: 10.1029/2021GL097211

Speer, K., Rintoul, S. R., & Sloyan, B. (2000). The Diabatic Deacon Cell. *Journal of Physical Oceanography*, *30*(12), 3212–3222. doi: 10.1175/1520-0485(2000)030⟨3212:TDDC⟩2.0.CO;2

Spira, T. (2024). *Antarctic Winter Water climatology overturning* [Software]. Github. (`https://github.com/theospira/WW_climatology`)

Spira, T., du Plessis, M., & Swart, S. (2023). *Processed hydrographic SO data, 2004-2021* [Dataset]. Zenodo. (https://zenodo.org/records/10258138) doi: 10.5281/zenodo.10258138
Spreen, G., Kaleschke, L., & Heygster, G. (2008). Sea ice remote sensing using AMSR-E 89-GHz channels. *Journal of Geophysical Research: Oceans*, *113*(C2). doi: 10.1029/2005JC003384
Stephenson Jr., G. R., Gille, S. T., & Sprintall, J. (2012). Seasonal variability of upper ocean heat content in Drake Passage. *Journal of Geophysical Research: Oceans*, *117*(C4). doi: 10.1029/2011JC007772
Stewart, K. D., & Haine, T. W. N. (2016). Thermobaricity in the Transition Zones between Alpha and Beta Oceans. *Journal of Physical Oceanography*, *46*(6), 1805–1821. doi: 10.1175/JPO-D-16-0017.1
Talley, L. (2013). Closure of the Global Overturning Circulation Through the Indian, Pacific, and Southern Oceans: Schematics and Transports. *Oceanography*, *26*(1), 80–97. doi: 10.5670/oceanog.2013.07
Tamsitt, V., Abernathey, R. P., Mazloff, M. R., Wang, J., & Talley, L. D. (2018). Transformation of Deep Water Masses Along Lagrangian Upwelling Pathways in the Southern Ocean. *Journal of Geophysical Research: Oceans*, *123*(3), 1994–2017. doi: 10.1002/2017JC013409
Tamsitt, V., Drake, H. F., Morrison, A. K., Talley, L. D., Dufour, C. O., Gray, A. R., ... Weijer, W. (2017). Spiraling pathways of global deep waters to the surface of the Southern Ocean. *Nature Communications*, *8*(1), 172. doi: 10.1038/s41467-017-00197-0
Tamsitt, V., England, M. H., Rintoul, S. R., & Morrison, A. K. (2021). Residence Time and Transformation of Warm Circumpolar Deep Water on the Antarctic Continental Shelf. *Geophysical Research Letters*, *48*(20), e2021GL096092. doi: 10.1029/2021GL096092
Tamsitt, V., Talley, L. D., Mazloff, M. R., & Cerovečki, I. (2016). Zonal Variations in the Southern Ocean Heat Budget. *Journal of Climate*, *29*(18), 6563–6579. doi: 10.1175/JCLI-D-15-0630.1
Tamura, T., Ohshima, K. I., & Nihashi, S. (2008). Mapping of sea ice production for Antarctic coastal polynyas. *Geophysical Research Letters*, *35*(7). doi: 10.1029/2007GL032903
Thompson, A. F., & Sallée, J.-B. (2012). Jets and Topography: Jet Transitions and the Impact on Transport in the Antarctic Circumpolar Current. *Journal of Physical Oceanography*, *42*(6), 956–972. doi: 10.1175/JPO-D-11-0135.1
Thompson, A. F., Stewart, A. L., Spence, P., & Heywood, K. J. (2018). The Antarctic Slope Current in a Changing Climate. *Reviews of Geophysics*, *56*(4), 741–770. doi: 10.1029/2018RG000624
Toole, J. M. (1981). Sea ice, winter convection, and the temperature minimum layer in the Southern Ocean. *Journal of Geophysical Research: Oceans*, *86*(C9), 8037–8047. doi: 10.1029/JC086iC09p08037
Treasure, A. M., Roquet, F., Ansorge, I. J., Bester, M. N., Boehme, L., Bornemann, H., ... de Bruyn, P. N. (2017). Marine Mammals Exploring the Oceans Pole to Pole: A Review of the MEOP Consortium. *Oceanography*, *30*(2), 132–138.
van der Boog, C. G., Dijkstra, H. A., Pietrzak, J. D., & Katsman, C. A. (2021). Double-diffusive mixing makes a small contribution to the global ocean circulation. *Communications Earth & Environment*, *2*(1), 1–9. doi: 10.1038/s43247-021-00113-x
van Sebille, E., Spence, P., Mazloff, M. R., England, M. H., Rintoul, S. R., & Saenko, O. A. (2013). Abyssal connections of Antarctic Bottom Water in a Southern Ocean State Estimate. *Geophysical Research Letters*, *40*(10), 2177–2182. doi: 10.1002/grl.50483
Vernet, M., Geibert, W., Hoppema, M., Brown, P. J., Haas, C., Hellmer, H. H.,

… Verdy, A. (2019). The Weddell Gyre, Southern Ocean: Present Knowledge and Future Challenges. *Reviews of Geophysics*, *57*(3), 623–708. doi: 10.1029/2018RG000604

Viglione, G. A., Thompson, A. F., Flexas, M. M., Sprintall, J., & Swart, S. (2018). Abrupt Transitions in Submesoscale Structure in Southern Drake Passage: Glider Observations and Model Results. *Journal of Physical Oceanography*, *48*(9), 2011–2027. doi: 10.1175/JPO-D-17-0192.1

von Kármán, T. (1931). Mechanische Ähnlichkeit und turbulenz. *Proceedings of the Third International Congress on Applied Mechanics*, *1*, 85-93. (Publisher: Sveriges Litografiska Tryckerier)

Wang, R., Nan, F., Yu, F., & Wang, B. (2022). Subantarctic Mode Water Variations in the Three Southern Hemisphere Ocean Basins During 2004–2019. *Journal of Geophysical Research: Oceans*, *127*(7), e2021JC017906. doi: 10.1029/2021JC017906

Waterhouse, A. F., MacKinnon, J. A., Nash, J. D., Alford, M. H., Kunze, E., Simmons, H. L., … Lee, C. M. (2014). Global Patterns of Diapycnal Mixing from Measurements of the Turbulent Dissipation Rate. *Journal of Physical Oceanography*, *44*(7), 1854–1872. doi: 10.1175/JPO-D-13-0104.1

Whalen, C. B., Talley, L. D., & MacKinnon, J. A. (2012). Spatial and temporal variability of global ocean mixing inferred from Argo profiles. *Geophysical Research Letters*, *39*(18). doi: 10.1029/2012GL053196

Whitworth, T., Nowlin, W. D., Orsi, A. H., Locarnini, R. A., & Smith, S. G. (1994). Weddell Sea shelf water in the Bransfield Strait and Weddell-Scotia Confluence. *Deep Sea Research Part I: Oceanographic Research Papers*, *41*(4), 629–641. doi: 10.1016/0967-0637(94)90046-9

Wilson, E. A., Riser, S. C., Campbell, E. C., & Wong, A. P. S. (2019). Winter Upper-Ocean Stability and Ice–Ocean Feedbacks in the Sea Ice–Covered Southern Ocean. *Journal of Physical Oceanography*, *49*(4), 1099–1117. doi: 10.1175/JPO-D-18-0184.1

Wilson, E. A., Thompson, A. F., Stewart, A. L., & Sun, S. (2022). Bathymetric Control of Subpolar Gyres and the Overturning Circulation in the Southern Ocean. *Journal of Physical Oceanography*, *52*(2), 205–223. doi: 10.1175/JPO-D-21-0136.1

Wong, A. P. S., & Riser, S. C. (2011). Profiling Float Observations of the Upper Ocean under Sea Ice off the Wilkes Land Coast of Antarctica. *Journal of Physical Oceanography*, *41*(6), 1102–1115. doi: 10.1175/2011JPO4516.1

Wong, A. P. S., Wijffels, S. E., Riser, S. C., Pouliquen, S., Hosoda, S., Roemmich, D., … Park, H.-M. (2020). Argo Data 1999–2019: Two Million Temperature-Salinity Profiles and Subsurface Velocity Observations From a Global Array of Profiling Floats. *Frontiers in Marine Science*, *7*.

Wu, L., Jing, Z., Riser, S., & Visbeck, M. (2011). Seasonal and spatial variations of Southern Ocean diapycnal mixing from Argo profiling floats. *Nature Geoscience*, *4*(6), 363–366. doi: 10.1038/ngeo1156

Xia, X., Hong, Y., Du, Y., & Xiu, P. (2022). Three Types of Antarctic Intermediate Water Revealed by a Machine Learning Approach. *Geophysical Research Letters*, *49*(21), e2022GL099445. doi: 10.1029/2022GL099445

Zilberman, N. V., Roemmich, D. H., & Gille, S. T. (2017). The East Pacific Rise current: Topographic enhancement of the interior flow in the South Pacific Ocean. *Geophysical Research Letters*, *44*(1), 277–285. doi: 10.1002/2016GL069039